

NACA RM No. A8E06

A 8 E 06

6290

~~CONFIDENTIAL~~
NACA

0142973

TECH LIBRARY KAFB, NM

RESEARCH MEMORANDUM

INVESTIGATION OF WING CHARACTERISTICS AT A MACH NUMBER
OF 1.53. III - UNSWEPT WINGS OF DIFFERING
ASPECT RATIO AND TAPER RATIO

By Jack N. Nielsen, Frederick H. Matteson,
and Walter G. Vincenti

Ames Aeronautical Laboratory
Moffett Field, Calif.

CLASSIFIED DOCUMENT

This document contains classified information affecting the National Defense of the United States within the meaning of the Espionage Act, Title 18, U.S.C., Sec. 793 and 794, and its transmission or the revelation of its contents in any manner to an unauthorized person is prohibited by law. Information contained herein is to be imparted only to persons authorized to receive naval services of the United States, including civilian officers and employees of the Government who have a legitimate interest therein, and to United States citizens who, in the interest of the national defense, are loyal and discretion who of necessity must be informed thereof.

**NATIONAL ADVISORY COMMITTEE
FOR AERONAUTICS**

WASHINGTON

June 21, 1948

~~CONFIDENTIAL~~

3/9.98/13

Classification cancelled (or changed to) UNCLASSIFIED
By Authority of NASA Tech Pub Announcement # 653
(OFFICER AUTHORIZED TO CHANGE)
By 1 Dec 53
NAME [Signature]
GRADE OF OFFICER MAKING CHANGE
DATE 12 Apr 61



0142973

NACA RM No. A8E06

NATIONAL ADVISORY COMMITTEE FOR AERONAUTICS

RESEARCH MEMORANDUM

INVESTIGATION OF WING CHARACTERISTICS AT A MACH NUMBER

OF 1.53. III - UNSWEPT WINGS OF DIFFERING

ASPECT RATIO AND TAPER RATIO

By Jack N. Nielsen, Frederick H. Matteson,
and Walter G. Vincenti

SUMMARY

As the third part of a general study of wing characteristics at supersonic speed, wind-tunnel tests were conducted of seven models forming two series of wings: (1) a series of taper ratio 0.5 and differing aspect ratio and (2) a series of aspect ratio 4 and differing taper ratio. All wings had an isosceles-triangle airfoil section 5-percent-thick and an unswept midchord line. Measurements were made of lift, drag, and pitching moment at a Mach number of 1.53 and a Reynolds number of 0.75 million. The experimental results were analyzed and compared with the characteristics calculated by means of linear theory.

The aerodynamic parameters generally varied with aspect ratio and taper ratio in the manner indicated by the linear theory. The majority of the aerodynamic parameters showed considerable variation with aspect ratio in the low-aspect-ratio range only. The parameters showed no appreciable change with taper ratio for the aspect ratio of 4. (This does not preclude the possibility of appreciable taper-ratio effects at lower aspect ratios.)

The measured values of the lift-curve slope were in close accord with the theoretical values for all the wings, but the experimental angles of zero lift were consistently higher than those given by linear theory mainly because of higher-order pressure effects neglected in linear theory. Both lift-curve slope and angle of zero lift increased with increase in aspect ratio.

The experimental values of moment-curve slope indicated positions of the aerodynamic center forward of those given by theory because of

~~CONFIDENTIAL~~

NACA RM No. A8E06

higher-order pressure effects and boundary-layer, shock-wave interaction near the trailing edge. The measured moment coefficients at zero lift were in good accord with the negative values calculated by linear theory. The aerodynamic center moved forward significantly with decrease in aspect ratio.

The drag curves were closely parabolic. The minimum drag increased slightly with increase in aspect ratio, and the drag-rise factor decreased. No decisive comparison could be made between experiment and theory for minimum drag because of the large but undetermined effects of support-body interference and skin friction upon this parameter. Rounding the leading edge of a rectangular wing of aspect ratio 4 to a radius of 0.25 percent of the chord increased the minimum drag coefficient by about 27 percent, but had no measurable effect on the lift and moment characteristics.

The experimental maximum lift-drag ratio remained between 5.6 and 6.4 over the complete range of plan forms.

INTRODUCTION

This report is the third and last of a series of reports covering a general study at a Mach number of 1.53 of wings differing in aspect ratio, taper ratio, sweep angle, and airfoil section. Part I of this series (reference 1) is a report on the effects of airfoil-section modifications on the aerodynamic characteristics of triangular wings of aspect ratio 2. Part II of the series (reference 2) is a report on the effects of sweep on the aerodynamic characteristics of wings of taper ratio 0.5.

In the present report, the aerodynamic characteristics for two families of unswept wings are discussed, the first family consisting of four wings of taper ratio 0.5 and differing aspect ratio, and the second family consisting of four wings of aspect ratio 4 and differing taper ratio. All wings have isosceles-triangle sections in the streamwise direction (maximum thickness at the midchord with a flat lower surface) and an unswept midchord line. With the exception of the data for one wing, all results are for a Reynolds number of 0.75 million. The experimental results for the wings are discussed in detail and compared with the calculated results of linear theory.

~~CONFIDENTIAL~~

SYMBOLS

Primary Symbols

A	aspect ratio (b^2/S)
$A\sqrt{M_o^2-1}$	effective aspect ratio
b	wing span
c	wing chord measured in streamwise direction
\bar{c}_a	mean aerodynamic chord $\left(\frac{2}{S} \int_0^{b/2} c^2 db\right)$
\bar{c}_g	mean geometric chord (S/b)
c_r	wing root chord
c_t	wing tip chord
C_D	total drag coefficient
C_{Dca}	pressure drag coefficient of cambered surface due to pressure field of flat-plate wing
C_{Dcc}	pressure drag coefficient of cambered surface due to own pressure field
C_{Df}	friction drag coefficient
ΔC_D	rise in drag coefficient above minimum drag $(C_D - C_{D_{min}})$
$C_{D_{min}}$	minimum total drag coefficient
$\frac{\Delta C_D}{(\Delta C_L)^2}$	drag-rise factor
C_{Dt}	pressure drag coefficient due to thickness
C_L	lift coefficient
$C_{L_{opt}}$	lift coefficient for maximum lift-drag ratio
ΔC_L	change in lift coefficient from value for minimum drag $(C_L - C_{L_{D=min}})$

4

CONFIDENTIAL

NACA RM No. A8E06

$\frac{dC_L}{d\alpha}$	lift-curve slope (per radian unless otherwise specified)
C_m	pitching-moment coefficient about centroid of plan-form area with mean aerodynamic chord as reference length
$\frac{dC_m}{dC_L}$	moment-curve slope
k_a	angle ratio $[\alpha_{\Delta L}/(\alpha - \alpha_{D=\min})]$
$\left(\frac{L}{D}\right)_{\max}$	maximum lift-drag ratio
M_o	free-stream Mach number
Re	Reynolds number based on mean geometric chord of wing
S	wing plan-form area
\bar{x}	distance back from leading edge of root chord to aerodynamic center
x_o	distance back from leading edge of root chord to centroid of plan-form area
$\frac{y_c}{c}$	maximum camber ratio of streamwise wing section
α	angle of attack
α_a	rearward inclination of force vector on flat-plate wing of same plan form as given complete wing
$\alpha_{\Delta L}$	rearward inclination of the change in resultant force corresponding to the change in lift coefficient ΔC_L
Λ_o	sweep angle of leading edge, degrees
$\frac{\Lambda_1}{2}$	sweep angle of midchord line, degrees
Λ_1	sweep angle of trailing edge, degrees
Subscripts	
$L=0$	value at zero lift
$D=\min$	value at minimum drag
$\alpha=0$	value at zero angle of attack

CONFIDENTIAL

- P refers to primary wing (i.e., flat-plate wing of same plan form as given complete wing)
- F refers to front-half component wing (i.e., flat-plate wing having same plan form as region ahead of ridge line)
- R refers to rear-half component wing (i.e., flat-plate wing having same plan form as region behind ridge line)

Additional Symbols Used In Appendix

- P_U upper-surface pressure coefficient
- P_L lower-surface pressure coefficient
- R.P. denotes real part of a complex function
- ΔP_a difference between lower-surface and upper-surface pressure coefficients due to primary loading
- ΔP_t difference between lower-surface and upper-surface pressure coefficients due to tips
- x streamwise distance measured from leading apex of wing
- y lateral distance measured from wing root chord
- f cotangent of leading-edge sweep angle (ctn Λ_0)
- g tangent of polar angle measured clockwise from wing tip
- h tangent of polar angle measured counterclockwise from wing root chord (y/x)
- s wing semispan
- St region of influence of wing tips on plan-form area

EXPERIMENTAL CONSIDERATIONS

The investigation was conducted in the Ames 1- by 3-foot supersonic wind tunnel No. 1. The experimental procedure employed throughout the general study is described in detail in Part I of the present series of reports (reference 1). Except where specifically

noted, all details of model construction and support, experimental technique, and reduction and correction of data may be taken as identical in the present report with those of Part I.

Models

Tests of two series of models are included in the present report. Photographs of the two series are shown in figures 1(a) and 1(b), and a picture of a wing mounted on the support body in the tunnel is shown in figure 1(c). Drawings of the models are given in figures 2(a) and 2(b), and a summary of the principal geometric characteristics of the models is given in table I. A drawing of the support body is given in Part I. All models had an area of 9 square inches.

The first wing series, called the aspect-ratio series, includes four models having a uniform taper ratio of 0.5 and varying in aspect ratio from 6 to 1. In order of decreasing aspect ratio, the models of the first series are designated U-1, U-2, U-3, and U-4, the letter U designating that the midchord line is unswept. The second wing series, called the taper-ratio series, includes four models having a uniform aspect ratio of 4 and varying in taper ratio (ratio of tip chord to root chord) from 1 to 0. In order of decreasing taper ratio, the models of the second series are designated U-5, U-6, and U-7. Model U-2 of taper ratio 0.5 and aspect ratio 4 is common to both series. All models have isosceles-triangle airfoil sections in the streamwise direction and an unswept midchord line.

The models were constructed of hardened tool steel, and in the main tests the leading and trailing edges were maintained sharp to less than 0.001-inch radius. In special tests to investigate the effect of leading-edge rounding, the leading edge of model U-5, a rectangular wing, was rounded successively to radii of 0.25 and 0.50 percent of the chord.

Corrections and Precision

For reasons discussed in Part I, no corrections have been applied to the data for the tare and interference effects of the support body. In other words, the experimental results are in each case for the wing-body combination rather than for the wing alone. In order to eliminate the effect of variation in balance-cap interference, the drag data have been reduced, as in Part I, to a common support-body base pressure equal to the static pressure of the free stream. The angles of attack have been corrected for stream angularity as

explained in Part I.

The precision of the present results is the same as that of the results of Part I (p. 13). Twist, which was appreciable for the wings of Part II, was negligible for the present wings. Bending was appreciable, however, for wing U-1, for which the tip chord was deflected three-quarters of an inch above the root chord at a Reynolds number of 0.46 million and an angle of attack of 8° . This bending limited the Reynolds number for this wing to 0.46 million. Although the bending was appreciable, there was no twist and no spanwise variation of the angle of attack.

THEORETICAL CONSIDERATIONS

General expressions for the lift, pitching-moment, and drag curves deduced from the assumptions of linear theory are given in Part I. For the wings of the present report, the values of individual terms in these expressions have been calculated insofar as practicable. Existing theoretical methods, in fact, permit first-order determination, exclusive of the effects of viscosity, of the aerodynamic characteristics of all the wings. The necessary integrations to determine the moment characteristics of wing U-4 would have entailed so much work, however, that they were not carried out. The theoretical calculations are otherwise complete.

As indicated in Part I, a given wing at angle of attack may be resolved into a symmetrical wing at zero angle of attack, a mean camber surface at zero angle of attack, and a flat lifting surface at the given angle of attack. According to linear theory, effects of thickness, camber, and angle of attack may then be considered separately in determining the pressure distribution — and hence the aerodynamic characteristics — of the given wing. The lift, pitching-moment, and drag curves are defined completely to the accuracy of the linear theory by the following seven quantities: $dC_L/d\alpha$, $\alpha_{L=0}$, dC_m/dC_L , $C_{mL=0}$, C_{Dmin} , $\Delta C_D/(\Delta C_L)^2$ and C_{LDmin} . The detailed methods used in calculating these quantities will be considered in the succeeding sections. (The detailed calculations were made in each case for an equivalent wing at a Mach number of $\sqrt{2}$, and the characteristics of the actual wing at the test Mach number of 1.53 were derived by means of the transformation rule described in reference 3.)

Lift and Moment Curves

As indicated by linear theory, the lift and moment curves are

~~CONFIDENTIAL~~

straight lines. The slopes $dC_L/d\alpha$ and dC_m/dC_L depend entirely on the pressure distribution on an inclined flat plate having the same plan form as the given wing.

The values of $dC_L/d\alpha$ and dC_m/dC_L for all the present wings except U-4 were determined directly from the integrated results of reference 4. The integrated results of this reference are subject to the restriction that the Mach lines from the leading edge of the root chord must intersect the trailing edge, and those from the leading edge of the tips must intersect the trailing edge on their own half of the plan form. For an unswept midchord line the restriction imposes the condition $A\sqrt{M_0^2-1} \geq 2$. Wing U-4 of aspect ratio unity does not meet the condition, and the lift-curve slope for this wing was determined from the results of the appendix. No determination of dC_m/dC_L was made for this wing.

The intercepts $C_{L_{\alpha=0}}$ and $C_{m_{\alpha=0}}$ depend entirely on the pressure distribution acting on the mean camber surface at zero angle of attack. The values of these quantities were determined from the following equations taken from Part II:

$$C_{L_{\alpha=0}} = -2 \left(\frac{y_c}{c} \right) \left[\left(\frac{dC_L}{d\alpha} \right)_P - \left(\frac{dC_L}{d\alpha} \right)_R \right] \quad (1)$$

$$C_{m_{\alpha=0}} = \frac{-2(y_c/c)}{c_a} \left[\left(\frac{dC_L}{d\alpha} \right)_P (x_0 - \bar{x}_P) + \left(\frac{dC_L}{d\alpha} \right)_R \left(\bar{x}_R + \frac{c_r}{2} - x_0 \right) \right] \quad (2)$$

These equations were derived by applying the superposition principle to the mean camber surface. In their present form they apply only to wings with the present type of mean camber surface having a supersonic ridge line at the midchord. The values of $(dC_L/d\alpha)_R$ in equations (1) and (2), as well as the values of $(dC_L/d\alpha)_F$ to be used in subsequent equations, were determined from the results of reference 4 for all the wings except U-4. For wing U-4, $(dC_L/d\alpha)_R$ was determined analytically using the well-known result of Busemann for the pressure field on the tip of a rectangular wing, and $(dC_L/d\alpha)_F$ was determined analytically by the method given in the appendix. The quantities $\alpha_{L=0}$ and $C_{m_{L=0}}$ were determined from the foregoing values with the aid of equations (2) and (4) of Part I. The values of $C_{m_{L=0}}$ are very nearly equal to the values of $C_{m_{\alpha=0}}$ for the present wings.

~~CONFIDENTIAL~~

Drag Curve

On the basis of linear theory, the drag curve is parabolic and can be written

$$C_D = C_{D_{min}} + \frac{\Delta C_D}{(\Delta C_L)^2} (C_L - C_{L_{D=min}})^2 \quad (3)$$

For the present wings, which necessarily have no leading-edge suction because of their supersonic leading edges, Part I gives for the minimum drag coefficient the equation

$$C_{D_{min}} = C_{D_f} + C_{D_t} + C_{D_{cc}} - \frac{1}{4(dC_L/d\alpha)} \left(C_{L_{\alpha=0}} + \frac{dC_{D_{ca}}}{d\alpha} \right)^2 \quad (4)$$

In calculating $C_{D_{min}}$ from equation (4) no skin friction was considered, and the theoretical values of $C_{D_{min}}$ thus represent only pressure drag. The values of C_{D_t} , the thickness drag coefficient, were taken from the charts of reference 3, and the values of $C_{D_{cc}}$ and $dC_{D_{ca}}/d\alpha$ were determined from the following equations taken from Part II:

$$C_{D_{cc}} = 4 \left(\frac{y_c}{c} \right)^2 \left[\left(\frac{dC_L}{d\alpha} \right)_F + \left(\frac{dC_L}{d\alpha} \right)_R - \left(\frac{dC_L}{d\alpha} \right)_P \right] \quad (5)$$

$$\frac{dC_{D_{ca}}}{d\alpha} = 2 \left(\frac{y_c}{c} \right) \left[\left(\frac{dC_L}{d\alpha} \right)_F - \left(\frac{dC_L}{d\alpha} \right)_P \right] \quad (6)$$

The values of $C_{D_{cc}}$ and C_{D_t} are equal for each of the present wings except U-4. It can be shown that, for C_{D_t} to be equal to $C_{D_{cc}}$, the increment in $C_{D_{cc}}$ or C_{D_t} attributable to the tips must be identically zero. As discussed in reference 3, the increment in C_{D_t} attributable to the tips is zero for wings of the present type when the Mach line originating at the leading edge of the tip intersects the trailing edge on its own half of the plan form. For an unswept midchord line, this restriction also imposes the limitation $A\sqrt{M_0^2-1} \geq 2$, so that for wing U-4 $C_{D_{cc}}$ and C_{D_t} are not equal.

With regard to the value of $dC_{Dca}/d\alpha$, reference 4 shows that $(dC_L/d\alpha)_F$ equals $(dC_L/d\alpha)_R$ for all the present wings except U-4. For wing U-4 this equality was found in the analytical determinations of $(dC_L/d\alpha)_F$ and $(dC_L/d\alpha)_R$. Thus, from equations (1) and (6), $dC_{Dca}/d\alpha$ equals $C_{L\alpha=0}$ and the last term in equation (4) for the minimum drag coefficient is simply $(C_{L\alpha=0})^2/(dC_L/d\alpha)$. This component of the drag is very small and could for all practical purposes be neglected, at least for the present wings.

The second quantity in equation (3) for the drag coefficient is $\Delta C_D/(\Delta C_L)^2$, the drag-rise factor. It was determined, as in Part II, from the relationship

$$\frac{\Delta C_D}{(\Delta C_L)^2} = \frac{k_a}{(dC_L/d\alpha)} \quad (7)$$

where k_a is equal to the rearward inclination of the force on the flat lifting surface as a fraction of the angle of attack. In accordance with the discussion of leading-edge suction on page 17 of Part I, k_a is unity for the present wings with supersonic leading edges, so that the drag-rise factor for each wing is simply the reciprocal of the lift-curve slope.

The remaining fixed quantity in equation (3) for the drag curve is $C_{LD=min}$, which according to equation (9) of Part II is

$$C_{LD=min} = \left(\frac{y_c}{c}\right) \left[\left(\frac{dC_L}{d\alpha}\right)_R - \left(\frac{dC_L}{d\alpha}\right)_F \right] \quad (8)$$

For all the present wings $(dC_L/d\alpha)_R$ equals $(dC_L/d\alpha)_F$; therefore, $C_{LD=min}$ is zero.

To summarize the limitations of the foregoing equations, equations (1), (2), (5), (6), and (8) apply only to uniformly tapered wings with supersonic ridge lines at the midchord and the present type of mean camber surface. Equations (4), (5), (6), and (8) are subject to the limitation that the leading edge be supersonic.

RESULTS AND DISCUSSION

The experimental values of the lift, drag, and pitching-moment coefficients together with the lift-drag ratio are given for wings

U-1 to U-7 in figures 3(a) to 3(g), respectively. As in Parts I and II, the coefficients are based on the plan-form area of the wings, including that portion of the plan form blanketed by the support body. Pitching-moment coefficients are taken about a transverse axis through the centroid of the plan form with the mean aerodynamic chord as reference length. All the data presented are for a test Mach number of 1.53 and, except for the case of wing U-1, are for a Reynolds number of 0.75 million based on the mean geometric chord. The data for wing U-1 are presented for a Reynolds number of 0.46 million, the highest attainable with this wing because of bending. It is believed, however, that the data for wing U-1 are comparable with the data for the other wings of the aspect-ratio series. Subsequent cross plots bear out this belief. The results of testing wing U-5 of rectangular plan form with the leading edge rounded to 0.25 percent chord are given in figure 4.

Theoretical curves obtained as described in the preceding section are included in figures 3(a) to 3(g) with the exception of the moment curve for wing U-4. The curves shown for the drag coefficient and the lift-drag ratio include only pressure drag.

The values of the aerodynamic parameters determined from the faired curves of figure 3 are summarized in table II at the end of the text together with the calculated theoretical values. In each instance, the value determined from the faired curve is given first and the corresponding theoretical value is indicated in parentheses directly below. The theoretical values of the section parameters calculated by means of the available higher-order, two-dimensional theories are also summarized in table II.

To facilitate comparison and to show trends, the experimental and theoretical values of the aerodynamic parameters are cross-plotted against aspect ratio for the aspect-ratio series and against taper ratio for the taper-ratio series in figures 5 to 14. It should be remembered that, in the case of the experimental quantities, the points represent values determined from a faired curve and not actual test points. On the cross plots for the aspect-ratio series, the values of the aerodynamic coefficients determined for the airfoil section by the linear theory are also indicated. These values correspond to $A = \infty$ and represent asymptotic values for this wing series.

It should be remembered throughout the succeeding discussion that the experimental results are in each case for a wing-body combination, while the theoretical characteristics are for the wing alone. As explained in Part I (p. 10), the effect of the slender

support body used here is probably small insofar as the experimental lift and moment are concerned. It may, however, be considerable with regard to the minimum drag. The minimum drag results must therefore be regarded as primarily of qualitative significance in comparison with the theoretical values. For the present wings, the effect of the support body is probably less than for the wings of Part I, since the fraction of the total wing area enclosed by the support body is less for the present wings than for the wings of Part I.

Lift

Although the lift curves of figure 3 show a slight tendency toward upward curvature at high angles of attack, they may be considered essentially linear. (On the basis of first- and second-order section theories, the lift curve is linear. However, the shock-expansion method indicates upward curvature at the high lift coefficients.) The lift curves of the present wings are thus well represented by the slope and intercept values of table II. The experimental and theoretical values of lift-curve slope and angle of zero lift are cross-plotted in figure 5 for the aspect-ratio series and in figure 6 for the taper-ratio series.

Lift-curve slope.— Figure 5(a) shows that the experimental lift-curve slope for the aspect-ratio series asymptotically approaches the section value at high aspect ratios and tends toward zero at an aspect ratio of zero. For the taper-ratio series, figure 6(a) shows no appreciable variation of lift-curve slope with taper ratio either experimentally or theoretically. The effect of taper ratio would, however, probably be appreciable for wings of lower aspect ratio. For both wing series the experimental and theoretical values are in excellent accord.

The relatively low values of lift-curve slope at low aspect ratios are caused largely by a loss of lift within the tip Mach cones. As pointed out in the appendix, this tip effect causes a reduction in theoretical lift-curve slope for wing U-4 at $M = 1.53$ from 0.0552 without tip effect to 0.0337 with it, a reduction of about 39 percent.

It is probable that the almost exact agreement noted between experiment and theory is fortuitous. The effect of boundary-layer, shock-wave interaction at the trailing edge (see Part II and later discussion of angle of zero lift) is normally to reduce the experimental values of lift-curve slope slightly below the theoretical

values for inviscid flow, so that precise agreement is not to be expected. Also, because the experimental data are for wing-body combinations, some difference between the experimental values and the theoretical values for the wing alone is to be anticipated.

Angle of zero lift.— For the aspect-ratio series the values of $\alpha_{L=0}$ shown in figure 5(b) vary from about 0.5° at an aspect ratio of 6 to about -0.5° at an aspect ratio of unity. Thus the effect of decrease in aspect ratio is to cause a decrease in angle of zero lift for wings of the present cambered airfoil section. No appreciable effect of taper ratio on the value of $\alpha_{L=0}$ for wings of aspect ratio 4 is exhibited by the curves of figure 6(b). The theoretical trends of $\alpha_{L=0}$ with changes in aspect ratio and taper ratio follow closely the experimental trends, but the experimental values are about 0.5° greater than the theoretical values.

The decrease in angle of zero lift with decrease in aspect ratio, both theoretically and experimentally, is readily explained by the following relationship obtained with the help of equation (1):

$$\alpha_{L=0} = 2 \left(\frac{y_c}{c} \right) \left[1 - \frac{(dC_L/d\alpha)_R}{(dC_L/d\alpha)_P} \right] \quad (9)$$

In this equation $(dC_L/d\alpha)_R$ is the lift-curve slope of the rear-half wing, which has twice the aspect ratio of the primary wing. In the high-aspect-ratio range, there is little effect of aspect ratio on lift-curve slope, and the lift-curve-slope ratio in equation (9) is nearly unity. Consequently, in this range $\alpha_{L=0}$ is small. In the low-aspect-ratio range, where lift-curve slope changes appreciably with aspect ratio, the rear-half component wing will have a much greater slope than the primary wing. Therefore, in this range the lift-curve-slope ratio will be considerably greater than unity, and $\alpha_{L=0}$ will be large and negative.

The difference between the experimental and theoretical values of $\alpha_{L=0}$ is due largely to higher-order pressure effects neglected in linear theory. As in table II, the section value of $\alpha_{L=0}$ is 0° on the basis of linear theory, while it is 0.36° on the basis of second-order theory. Thus for wings of high aspect ratio, which are subject to approximately two-dimensional flow over much of their area, most of the above difference between experiment and theory can be ascribed to the inability of linear theory to predict accurately the section value of the angle of zero lift. This shortcoming of the linear theory has also been noted in Parts I and II.

Another effect which contributes to the 0.5° difference between the experimental and theoretical values of $\alpha_{L=0}$ is interaction between the upper-surface boundary layer and the oblique trailing-edge shock wave as reported originally by Ferri (reference 5). The upper-surface boundary layer approaching the trailing edge separates because the pressure rise through the trailing-edge shock wave is propagated forward through the boundary layer. Behind the point of separation the pressures are higher than they would be for an unseparated layer. On a cambered section, this effect occurs on the upper surface even at small angles of attack and causes $\alpha_{L=0}$ to be higher than it would be in the absence of viscosity. As will be seen, the interaction also has an influence on other aerodynamic quantities.

Pitching Moment

Straight lines have been faired through the moment data of figure 3 for all the wings, even though there is a slight, consistent tendency toward upward curvature at negative lift coefficients. (In Part II it was surmised that this tendency may be due to a small, systematic error in the moment measurements near zero lift.) The moment characteristics of the present wings are well represented by the slope and intercept values of the faired curves as tabulated in table II. The experimental and theoretical values of moment-curve slope and moment coefficient at zero lift are cross-plotted in figure 7 for the aspect-ratio series and in figure 8 for the taper-ratio series.

Moment-curve slope.— The data of figure 7(a) indicate that dC_m/dC_L increases significantly with decrease in aspect ratio, corresponding to considerable forward movement of the aerodynamic-center position. For instance, the value of 0.056 for dC_m/dC_L of wing U-1 (aspect ratio 6) places its aerodynamic center 5.6 percent of the mean aerodynamic chord in front of the centroid; whereas the aerodynamic center of wing U-4 (aspect ratio unity) is 20 percent of the mean aerodynamic chord in front of the centroid. This trend is also exhibited by the theoretical curve in figure 7(a), but the experimental curve is displaced upward from the theoretical curve by a nearly constant amount. No appreciable change in moment-curve slope due to changes in taper ratio are shown in figure 8(a). The experimental curve is again displaced vertically from the theoretical curve by an amount approximately equal to that for the aspect-ratio series.

The tendency for the aerodynamic center to move forward with decrease in aspect ratio is due primarily to the appreciable losses

CONFIDENTIAL

of lift that occur over the rear portion of the wing within the tip Mach cones. This loss of lift, which is described in the appendix, becomes relatively greater as the aspect ratio decreases and causes the forward movement of the aerodynamic center.

A large part of the observed difference between the experimental and theoretical values of dC_m/dC_L for the wings of large aspect ratio, which are subjected to approximately two-dimensional flow over most of their plan form, can be attributed to higher-order pressure effects neglected in linear theory. As a numerical illustration, consider wing U-1, which has an experimental moment-curve slope of 0.056 compared with a theoretical value of 0.007, a difference of about 0.050. As seen in table II, the effect of including second-order pressure terms in the calculation of dC_m/dC_L for the present airfoil section is to increase the theoretical value of dC_m/dC_L from zero to 0.032, about two-thirds of the observed difference. It is probable that half or more of the difference between experiment and theory for the other wings is due to second-order pressure effects. Boundary-layer, shock-wave interaction near the trailing edge may contribute to the remainder. This effect causes a local loss of lift which increases with angle of attack, thereby increasing dC_m/dC_L .

The moment data of figure 7(a), which indicate forward movement of the aerodynamic center with decrease in aspect ratio for constant Mach number, may be interpreted as illustrating the similar forward movement to be expected as the Mach number is decreased for a wing of given aspect ratio. Such an interpretation follows from the result of linear theory that the aerodynamic-center position for a wing of the aspect-ratio series depends only on the effective aspect ratio $A\sqrt{M_0^2-1}$, making a decrease in Mach number at constant aspect ratio equivalent to a decrease in aspect ratio at constant Mach number.

Moment coefficient at zero lift.— Both the experimental and theoretical values of $C_{mL=0}$ shown in figures 7(b) and 8(b) exhibit no appreciable change with either aspect ratio or taper ratio. The experimental values are, however, less negative than the theoretical values by a small but consistent amount. The difference cannot be attributed to higher-order pressure effects, since there is no appreciable difference between the section values of $C_{mL=0}$ calculated on the basis of linear theory and on the basis of second-order theory. It is probable that the difference is due to boundary-layer, shock-wave interaction. Any loss of lift near the trailing edge as a result of interaction of the upper-surface boundary layer and the trailing-edge shock wave, such as was discussed in connection with

the angle of zero lift, would tend to increase the pitching moment at zero lift.

Drag and Lift-Drag Ratio

Analysis of the data indicates that the experimental drag curves of figure 3 have in each case approximately parabolic shape as predicted by equation (3). Thus, the present drag curves can be defined by the values of the minimum drag coefficient $C_{D_{min}}$, the lift coefficient for minimum drag $C_{L_{D_{min}}}$, and the drag-rise factor $\Delta C_D / (\Delta C_L)^2$. The experimental and theoretical values of these quantities are summarized in table II, together with the values k_a , $C_{L_{opt}}$, and $(L/D)_{max}$. The various quantities involved in discussion of the drag and lift-drag ratio have been cross-plotted against aspect ratio and taper ratio in figures 9 to 14. In all cases the theoretical values are for no skin friction.

Minimum drag coefficient.— The experimental values of $C_{D_{min}}$ in figure 9(a) show small but definite decrease with decrease in aspect ratio, but the corresponding theoretical values show little variation with aspect ratio. No appreciable effects of taper ratio on $C_{D_{min}}$ are indicated either experimentally or theoretically by the curves of figure 10(a), although the results of reference 3 indicate that appreciable effects of taper ratio would occur at lower aspect ratios. Generally speaking, the experimental values of $C_{D_{min}}$ are 0.004 to 0.007 higher than the theoretical values.

A large part of the difference between the experimental and theoretical values of $C_{D_{min}}$ can be ascribed to skin friction. Although no determination of the actual areas of laminar and turbulent flow was made for the present wings by the liquid-film method as in Part I, it is thought that the flow is mostly laminar because of the small areas of adverse gradient for most of the wings. At a Reynolds number of 0.75 million, laminar skin friction would account for an increment in $C_{D_{min}}$ of about 0.003. The remainder of the 0.004 to 0.007 difference may be attributed to the partially compensating effects of support-body drag, mutual interference between the wing and support body, and shock-wave, boundary-layer interaction.

The effect of rounding the leading edge of the rectangular wing (U-5) is shown by a comparison of figure 3(e) for the sharp-edged wing with figure 4 for the wing with a leading-edge radius of 0.25 percent of the chord. (This amount of rounding gave the present isosceles-triangle section a nose radius comparable to that for an

NACA low-drag section of equal thickness ratio.) Comparison of the figures shows that rounding had the appreciable effect of increasing $C_{D_{min}}$ by an increment which was about 27 percent of $C_{D_{min}}$ for the sharp-edged wing. Further rounding of the leading edge to a radius of 0.50 percent of the chord further increased $C_{D_{min}}$ by the same increment. There was no noticeable effect on the other measured aerodynamic quantities. This is in contrast to the results of Parts I and II where the minimum drag of wings with a highly swept (subsonic) leading edge was not altered by rounding.

Lift coefficient for minimum drag.— The experimental values of $C_{L_{D=min}}$ in figure 9(b) exhibit some variation with aspect ratio; the experimental values in figure 10(b) exhibit practically no variation with taper ratio. Quantitatively, the values of $C_{L_{D=min}}$ vary from 0.02 to 0.04 for the seven present wings. These experimental results are not in accord with the theoretical result that $C_{L_{D=min}}$ is constant at zero for all the wings. (It is interesting to note that over the wide range of plan forms covered by the present wings $C_{D_{min}}$ varied within the narrow limits of 0.7° to 0.9° .)

Higher-order pressure effects neglected in linear theory account for part of the difference between the experimental and theoretical values of $C_{L_{D=min}}$. With reference to table II, it is seen that $C_{L_{D=min}}$ for the present section is zero on the basis of linear theory; whereas it is 0.014 on the basis of the shock-expansion method. It is also likely that boundary-layer, shock-wave interaction contributes a significant part of the observed difference. At all positive angles of attack for the present wings, there is a shock wave at the trailing edge on the upper surface and an expansion on the lower surface. The separation which results from interaction between the boundary layer and the shock wave on the upper surface will cause an increase in pressure over the rear part of the surface and a decrease in drag. As the angle of attack increases from zero, this effect increases, tending to make the reduction in drag progressive. This effect, which is in opposition to the usual increase in drag with increase in angle of attack, will have considerable influence on the value of $C_{L_{D=min}}$. Thus it is possible to say that both higher-order pressure effects and interaction have appreciable influence on $C_{L_{D=min}}$. These effects are of importance since they are reflected in the value of the maximum lift-drag ratio.

Drag-rise factor.— The rise in drag as the lift coefficient departs from the value for minimum drag is specified for a parabolic drag curve by the value of the drag-rise factor $\Delta C_D/(\Delta C_L)^2$. The

values of $\Delta C_D/(\Delta C_L)^2$ have been determined, following the method of Part II, by evaluating the slope of a straight line faired through the experimental points on plots of $C_D - C_{D_{\min}}$ versus $(C_L - C_{L_{D=\min}})^2$. The values so obtained are plotted against aspect ratio in figure 11(a) and against taper ratio in figure 12(a).

As pointed out in Part II, the drag-rise factor given by linear theory depends on the lift-curve slope and the rearward inclination of the change in resultant force corresponding to the change in lift ΔC_L . This latter quantity is specified by the angle ratio k_a , which is defined as the inclination of the change in resultant force divided by the accompanying change in angle of attack, that is,

$$k_a = \frac{\alpha_{\Delta L}}{(\alpha - \alpha_{D=\min})} \approx \frac{\Delta C_D / \Delta C_L}{(\alpha - \alpha_{D=\min})} \quad (10)$$

As in Part II, average experimental values of k_a have been determined in accordance with this definition by evaluating the slopes of straight lines faired through plots of the experimental values of ΔC_D versus $(\Delta C_L) \times (\alpha - \alpha_{D=\min})$. To the extent that the experimental drag curve is parabolic and the experimental lift curve is linear, the experimental values of $\Delta C_D/(\Delta C_L)^2$, k_a , and $dC_L/d\alpha$ will satisfy equation (7). The experimental values of k_a for the aspect-ratio series are given in figure 11(b) and the values for the taper-ratio series are given in figure 12(b). The theoretical value of k_a , which is evaluated as indicated just after equation (7), is unity for all of the present wings.

An examination of figures 11(b) and 12(b) reveals that there is no significant variation of k_a experimentally or theoretically with either aspect ratio or taper ratio. The experimental values are greater than the theoretical value of unity but by never more than 10 percent. This indicates that no leading-edge suction is developed by the present wings in accordance with the prediction of theory for wings with a supersonic leading edge. The result shows that the rearward inclination of the change in resultant force corresponding to ΔC_L is, in fact, slightly greater than the corresponding change in angle of attack. This condition may be due to a slight increase in skin friction with increasing angle of attack.

Figure 11(a) shows that experimentally $\Delta C_D/(\Delta C_L)^2$ decreases at a decreasing rate with increasing aspect ratio and that the theoretical and experimental values are in excellent accord. The theoretical and experimental values of $\Delta C_D/(\Delta C_L)^2$ in figure 12(a)

show no change with taper ratio and are also in excellent accord. The close agreement between experiment and theory for the drag-rise factor is an over-all consequence of the facts that the lift curves are linear, the drag curves are parabolic, and the theoretical and experimental values of k_a and $dC_L/d\alpha$ are in close accord. Since the drag-rise factor is inversely proportional to the lift-curve slope when k_a is unity (equation (7)), the experimental variation of $\Delta C_D/(\Delta C_L)^2$ with aspect ratio shown in figure 11(a) is simply a reflection of the experimental variation of $dC_L/d\alpha$ noted in figure 5(a).

Lift-drag ratio.— For a parabolic drag curve the maximum lift-drag ratio is given by

$$\left(\frac{L}{D}\right)_{\max} = \frac{1}{2 \left[\Delta C_D/(\Delta C_L)^2 \right] \left[C_{L_{\text{opt}}} - C_{L_{D=\min}} \right]} \quad (11)$$

where the optimum lift coefficient is given by

$$C_{L_{\text{opt}}} = \sqrt{\frac{C_{D_{\min}}}{[\Delta C_D/(\Delta C_L)^2]} + (C_{L_{D=\min}})^2} \quad (12)$$

Equations (11) and (12) demonstrate the dependency of $(L/D)_{\max}$ on the three primary characteristics which geometrically determine the drag parabola, $C_{D_{\min}}$, $\Delta C_D/(\Delta C_L)^2$, and $C_{L_{D=\min}}$. The experimental values of these quantities satisfy the above equations approximately since the experimental drag curves are nearly parabolic. Theoretical values of $C_{L_{\text{opt}}}$ and $(L/D)_{\max}$ have been determined by the above formulas and are given together with the experimental values of these quantities in table II. It should be remembered that the effect of skin friction has been omitted in computing the theoretical values. The theoretical and experimental values are cross-plotted against aspect ratio in figure 13 and against taper ratio in figure 14.

An examination of figures 13 and 14 reveals that the experimental lift-drag ratio varies from 5.6 to 6.4. Above an aspect ratio of 2 the experimental maximum lift-drag ratio is nearly constant, but below this point it tends to decrease with decrease in aspect ratio. In the high-aspect-ratio range the experimental lift-drag ratios are less than the theoretical ones, but at an aspect ratio of unity the

~~CONFIDENTIAL~~

experimental value is greater than the theoretical. Theoretically and experimentally, the optimum lift coefficient increases at first with aspect ratio and then becomes constant at the higher aspect ratios. However, the experimental values of CL_{opt} are consistently greater than the theoretical values for all aspect ratios. There is little variation either theoretically or experimentally of $(L/D)_{max}$ and CL_{opt} with taper ratio. For all taper ratios the experimental values of $(L/D)_{max}$ are consistently less than the theoretical values, and the experimental values of CL_{opt} are consistently greater than the theoretical.

The variation of the theoretical values of CL_{opt} with aspect ratio can be explained by equation (12). In this equation $CL_{D=min}$ has a secondary effect on CL_{opt} ; and, since theoretically CD_{min} does not vary much with aspect ratio in the present range, changes in CL_{opt} are primarily due to change in $\Delta CD/(\Delta CL)^2$. Thus the theoretical variation of CL_{opt} in figure 13(b) is a reflection of the theoretical variation of $\Delta CD/(\Delta CL)^2$ in figure 11(a). The variation of $(L/D)_{max}$ with aspect ratio can similarly be explained by equation (11) in terms of the variation in drag-rise factor, optimum lift coefficient, and lift coefficient for minimum drag.

The differences between the theoretical and experimental values of CL_{opt} are due primarily to the differences in theoretical and experimental values of CD_{min} . This follows from equation (12), since $CL_{D=min}$ has little effect on CL_{opt} and since the theoretical and experimental values of $\Delta CD/(\Delta CL)^2$ are in good accord. Likewise, from equation (11), the differences between the theoretical and experimental values of $(L/D)_{max}$ are due to differences in the theoretical and experimental values of $(CL_{opt} - CL_{D=min})$. If boundary-layer, shock-wave interaction and higher-order pressure effects increase $CL_{D=min}$ above the theoretical value less than skin friction increases CL_{opt} , then the experimental lift-drag ratio will be less than the theoretical. This is the case for all the wings except U-4. For this wing the effect of increasing $CL_{D=min}$ is so favorable that the experimental $(L/D)_{max}$ is greater even than the theoretical $(L/D)_{max}$ without skin friction.

The present wings with camber have approximately twice the theoretical minimum pressure drag as the same wings would have if they were uncambered. The uncambered wings would have minimum drag at zero lift coefficient; whereas the cambered wings have their minimum drag experimentally at a positive lift coefficient. According to equations (11) and (12) camber would thus tend to decrease $(L/D)_{max}$ because of the increase in CL_{opt} accompanying

~~CONFIDENTIAL~~

increase in $C_{D_{min}}$, but would tend to increase $(L/D)_{max}$ because of the increase in $C_{L_{D=min}}$. These two effects are largely compensating. The use of cambered sections in the present investigation thus does not appreciably reduce $(L/D)_{max}$ as compared with what would probably be obtained for uncambered wings of the same thickness.

CONCLUSIONS

Tests were conducted at a Mach number of 1.53 and a Reynolds number of 0.75 million of seven wing models having isosceles-triangle wing sections with a maximum thickness of 5 percent. The wings, which all had unswept midchord lines, formed a wing series of aspect ratio 4 and various taper ratios and a wing series of taper ratio 0.5 and various aspect ratios. The investigation afforded the following conclusions:

1. The aerodynamic parameters varied with aspect ratio and taper ratio in the general manner indicated by theory.
2. The majority of the aerodynamic parameters showed considerable variation with aspect ratio in the low-aspect-ratio range only. The parameters showed no appreciable change with taper ratio for an aspect ratio of 4. (This does not preclude the possibility of appreciable taper-ratio effects at lower aspect ratios.)
3. For all the wings, the lift curves were linear, and the experimental and theoretical lift-curve slopes were in close accord. The lift-curve slope increased with increase in aspect ratio.
4. The experimental angles of zero lift were about $\frac{1}{2}^{\circ}$ higher than those given by the linear theory mainly because of higher-order pressure effects neglected in the linear theory. The angle of zero lift increased from negative to positive values with increase in aspect ratio.
5. The moment curves were approximately linear. The experimental slopes indicated positions of the aerodynamic center forward of the positions given by theory primarily because of higher-order pressure effects and boundary-layer, shock-wave interaction near the trailing edge. The aerodynamic center moved forward significantly with decrease in aspect ratio.
6. The measured values of the moment coefficient at zero lift did not vary appreciably with either aspect ratio or taper ratio,

and were in good accord with the negative values calculated by linear theory.

7. The drag curves were nearly parabolic. The minimum drag increased slightly with increase in aspect ratio. No decisive comparison could be made between experiment and theory for minimum drag because the undetermined effect of support-body interference and skin friction was known to be large.

8. The theoretical and experimental drag-rise factors were in close accord. The experimental drag-rise factors increased with decrease in aspect ratio.

9. The experimental values of maximum lift-drag ratio varied from 5.6 to 6.4.

10. Rounding the leading edge of the rectangular wing to a radius of 0.25 percent of the chord increased the minimum drag coefficient by about 27 percent but had no measurable effect on the lift and moment characteristics.

Ames Aeronautical Laboratory,
 National Advisory Committee for Aeronautics,
 Moffett Field, Calif.

APPENDIX

DETERMINATION OF LIFT-CURVE SLOPE FOR WING U-4

The results of reference 4, which have been used to determine the theoretical lift-curve slopes of all the present wings except U-4, applies to wings for which the Mach line emanating from the leading edge of the tip section intersects the trailing edge on its own half wing. For wing U-4, which does not fulfill this condition, a method suggested by Lagerstrom and applied by Cohen (reference 6) to highly swept wings has been used to determine the lift-curve slope.

The primary loading on the wing ΔP_a is taken as that corresponding to an infinite triangle, the leading edges of which include the leading edges of the wing. Within the tip Mach cones, the vertices of which are the extremities of the wing leading edge, there is induced by the tips a decrement in loading ΔP_t below the primary loading. It is to determine this decremental loading that the method suggested by Lagerstrom is used. With reference to the areas shown in figure 15, an expression for the lift-curve slope can be written

$$\frac{dC_L}{d\alpha} = \frac{\int_{S_1} \frac{\Delta P_a}{\alpha} dS_1 + \int_{S_2} \frac{\Delta P_a}{\alpha} dS_2 + \int_{S_3} \frac{\Delta P_a}{\alpha} dS_3 - \int_{S_t} \frac{\Delta P_t}{\alpha} dS_t}{S} \quad (A1)$$

The first three integrals represent the positive contribution of the primary loading to the lift-curve slope, and the last integral represents the negative contribution of the decremental loading induced by the tips.

Primary Loading Due to Infinite Triangle

For lifting surfaces with a supersonic leading edge, the upper- and lower-surface pressures are independent, and are equal in magnitude and opposite in sign. The lower surface of the infinite triangle giving the primary loading has a positive pressure and is inclined at $+\alpha$ radians to the flow. It is known from the results of reference 7 that two semi-infinite pressure sources extending from the leading apex to infinity, as shown in figure 15(a), will produce constant-slope wedge boundaries behind them. If the strength of the sources is adjusted so that the streamwise slope of the wedge is $+\alpha$ radians, then the pressure field on either face of the wedge will be the same as that on the lower surface of the infinite triangle. Thus, from the results of reference 7,

$$P_L = R.P. \frac{2\alpha \operatorname{ctn} \Lambda_0}{\pi \sqrt{\operatorname{ctn}^2 \Lambda_0 - 1}} \left\{ \cos^{-1} \left[\frac{1 - (\operatorname{ctn} \Lambda_0)(y/x)}{\operatorname{ctn} \Lambda_0 - (y/x)} \right] + \cos^{-1} \left[\frac{1 + (\operatorname{ctn} \Lambda_0)(y/x)}{\operatorname{ctn} \Lambda_0 + (y/x)} \right] \right\} \quad (A2)$$

Since $P_U = -P_L$ and $\Delta P_a = P_L - P_U$, the primary loading per radian is given by the equation

$$\frac{\Delta P_a}{\alpha} = R.P. \frac{4 \operatorname{ctn} \Lambda_0}{\pi \sqrt{\operatorname{ctn}^2 \Lambda_0 - 1}} \left\{ \cos^{-1} \left[\frac{1 - (\operatorname{ctn} \Lambda_0)(y/x)}{\operatorname{ctn} \Lambda_0 - (y/x)} \right] + \cos^{-1} \left[\frac{1 + (\operatorname{ctn} \Lambda_0)(y/x)}{\operatorname{ctn} \Lambda_0 + (y/x)} \right] \right\} \quad (A3)$$

A change of variables is introduced to simplify the analysis as follows:

$$f = \operatorname{ctn} \Lambda_0$$

$$h = y/x$$

~~CONFIDENTIAL~~

Equation (A3) then becomes

$$\frac{\Delta P_a}{\alpha} = R.P. \frac{4f}{\pi \sqrt{f^2-1}} \left[\cos^{-1} \left(\frac{1-fh}{f-h} \right) + \cos^{-1} \left(\frac{1+fh}{f+h} \right) \right] \quad (A4)$$

To obtain the contribution of the primary loading to the lift-curve slope, it is necessary to evaluate the first three integrals of equation (A1) by substituting the expression for $\Delta P_a/\alpha$ from equation (A4) and using the following expressions for the differential areas dS_1 , dS_2 , and dS_3 , which are taken as small triangles from the leading apex (fig. 15(a)):

$$\left. \begin{aligned} dS_1 &= \frac{s^2}{2h^2} dh \\ dS_2 &= \frac{s^2}{2h^2} dh \\ dS_3 &= \frac{c_r^2}{2} f^2 \frac{dh}{(f+h)^2} \end{aligned} \right\} \quad (A5)$$

In the evaluation of the first integral, the value of h varies from 1 to f . For this range of h , equation (A4) reduces to the simple equality

$$\frac{\Delta P_a}{\alpha} = \frac{4f}{\sqrt{f^2-1}} \quad (A6)$$

The expression for dS_1 from equation (A5) and the expression for $\Delta P_a/\alpha$ from equation (A6) are then substituted into the integral giving

$$\int_{S_1} \frac{\Delta P_a}{\alpha} dS_1 = 2 \int_1^f \frac{4f}{\sqrt{f^2-1}} \frac{s^2}{2h^2} dh \quad (A7)$$

Carrying through the integration, and substituting the limits then gives for the first integral

~~CONFIDENTIAL~~

$$\int_{S_1} \frac{\Delta P_a}{\alpha} dS_1 = \frac{4s^2(f-1)}{\sqrt{f^2-1}} \quad (A8)$$

In the evaluation of the second integral, the expression for $\Delta P_a/\alpha$ from equation (A4) is substituted into the integral together with the expression for dS_2 from equation (A5), and the integral is taken between the limits of h shown in figure 15(a). This gives

$$\int_{S_2} \frac{\Delta P_a}{\alpha} dS_2 = 2 \int_{\frac{fs}{fc_r-s}}^1 \frac{4f}{\pi\sqrt{f^2-1}} \left[\cos^{-1} \left(\frac{1-fh}{f-h} \right) + \cos^{-1} \left(\frac{1+fh}{f+h} \right) \right] \frac{s^2}{2h^2} dh \quad (A9)$$

Carrying out the integration and substituting the limits gives for the second integral

$$\begin{aligned} \int_{S_2} \frac{\Delta P_a}{\alpha} dS_2 = \frac{4fs^2}{\pi\sqrt{f^2-1}} & \left\{ \frac{c_r}{s} \cos^{-1} \left[\frac{1}{f} + \left(\frac{s}{c_r} \right) \left(\frac{f^2-1}{f^2} \right) \right] \right. \\ & \left. - \frac{\pi(f-1)}{f} - \frac{\left[2 \left(\frac{s}{c_r} \right) - f \right]}{f(s/c_r)} \cos^{-1} \left[\frac{1 - \left(\frac{s}{c_r} \right) \left(\frac{f^2+1}{f} \right)}{f - 2(s/c_r)} \right] \right\} \end{aligned} \quad (A10)$$

In the evaluation of the third integral, the expression for $\Delta P_a/\alpha$ from equation (A4) is substituted into the integral together with the expression for dS_3 from equation (A5), and the integral is taken between the limits of h shown in figure 15(a). Thus

$$\begin{aligned} \int_{S_3} \frac{\Delta P_a}{\alpha} dS_3 = 2 \int_0^{\frac{fs}{fc_r-s}} & \frac{4f}{\pi\sqrt{f^2-1}} \left[\cos^{-1} \left(\frac{1-fh}{f-h} \right) \right] \frac{c_r^2 f^2}{2} \frac{dh}{(f+h)^2} \\ & + 2 \int_0^{\frac{fs}{fc_r-s}} \frac{4f}{\pi\sqrt{f^2-1}} \left[\cos^{-1} \left(\frac{1+fh}{f+h} \right) \right] \frac{c_r^2 f^2}{2} \frac{dh}{(f+h)^2} \end{aligned} \quad (A11)$$

Carrying out the integration and substituting the limits gives for the third integral

$$\int_{S_3} \frac{\Delta P_a}{\alpha} dS_3 = \frac{4c_r^2 f}{\pi \sqrt{f^2-1}} \left\{ \frac{2(s/c_r)-f}{2} \cos^{-1} \left[\frac{1 - \left(\frac{s}{c_r}\right) \left(\frac{f^2+1}{f}\right)}{f-2(s/c_r)} \right] \right. \\
+ \frac{f(3-f^2)+2(s/c_r)(f^2-1)}{2(f^2-1)} \cos^{-1} \left[\frac{1}{f} + \left(\frac{s}{c_r}\right) \left(\frac{f^2-1}{f^2}\right) \right] \\
\left. + \frac{f(f^2-2)}{(f^2-1)} \cos^{-1} \left(\frac{1}{f}\right) + \frac{f}{\sqrt{f^2-1}} - \frac{f \sqrt{[1-f(s/c_r)]^2 - (s/c_r)^2}}{\sqrt{f^2-1}} \right\} \quad (A12)$$

Decremental Loading Due to Wing Tips

The lines of constant load for the primary loading are conical with respect to the leading apex and extend backwards to infinity. Since the loading off the wing between rays $h = fs/(fc_r-s)$ and $h = f$ can influence the wing pressures in region S_t (fig. 15(b)), it is necessary to find a solution which will identically duplicate this loading (or, considered as a decrement, will identically cancel this loading), and which will have zero contribution to the wing downwash. First a method of reproducing this loading with uniformly-loaded infinite triangles is considered.

With reference to figure 15(a), consider an infinite triangle, the vertex of which is at A and the sides of which extend to infinity along lines AB and AE. This infinite triangle is assigned the uniform loading $4f/\sqrt{f^2-1}$, the value of the primary loading in the interval $f \geq h \geq 1$. It thus reproduces identically the primary loading off the wing between the line pressure source and the Mach line. Between the Mach line and the ray $h = fs/(fc_r-s)$, the primary loading is less than $4f/\sqrt{f^2-1}$. Negative loading must therefore be superimposed onto the uniform loading of the previous infinite triangle in order to reproduce identically the primary loading in this region. Consider the infinite triangle, the vertex

of which is at D and the sides of which extend to infinity along lines DF and DE. This triangle is assigned the uniform negative loading $d(\Delta P_a/\alpha)$ as given by equation (A4). Point D is then allowed to move from point C to point E, and the negative loadings of all the infinite triangles the vertices of which lie in this interval are superimposed onto the loading of the infinite triangle with vertex at A. The primary loading off the wing between the Mach line and the ray $h = fs/(fc_r - s)$ will then be identically reproduced.

Lagerstrom in reference 4, using the conical flow method of Busemann, has determined the pressure field of a uniformly loaded infinite triangle of the present type which will not change the downwash on the wing. For the infinite triangle, the vertex of which is at A, the loading (per radian) is given by the equation

$$\left(\frac{\Delta P_t}{\alpha}\right)_0 = R.P. \frac{4f}{\pi \sqrt{f^2 - 1}} \cos^{-1} \left(\frac{2gf + g - f}{f + g} \right) \quad (A13)$$

The quantity $(\Delta P_t/\alpha)_0$ is considered as the decrement in wing loading due to canceling the primary loading on this infinite triangle. The variable g is indicated in figure 16(a). The infinitesimal decrement in wing loading due to the infinite triangles in the interval $1 \geq h \geq fs/(fc_r - s)$ by analogy with equation (A13) is given as

$$d\left(\frac{\Delta P_t}{\alpha}\right) = R.P. d\left(\frac{\Delta P_a}{\alpha}\right) \frac{1}{\pi} \cos^{-1} \left(\frac{2gh + g - h}{g + h} \right) \quad (A14)$$

or, using equation (A4),

$$d\left(\frac{\Delta P_t}{\alpha}\right) = R.P. \frac{8hf}{\pi^2 \sqrt{1-h^2} (f^2 - h^2)} \cos^{-1} \left(\frac{2gh + g - h}{g + h} \right) dh \quad (A15)$$

In evaluating the fourth and last integral of equation (A1), the contribution to the wing loading of each infinite triangle in the interval $1 \geq h \geq fs/(fc_r - s)$, as given by equation (A14), must be integrated over its region of influence on the wing, and then the sum contribution of all the triangles in the interval must be

determined. This sum contribution is then subtracted from the contribution given by equation (A13) integrated over its region of influence to give the fourth integral of equation (A1) in accordance with the equation

$$\int_{S_t} \left(\frac{\Delta P_t}{\alpha} \right) dS_t = \int_{S_t} \left(\frac{\Delta P_t}{\alpha} \right)_0 dS_t - \int \int_{S_t} d \left(\frac{\Delta P_t}{\alpha} \right) dS_t \quad (A16)$$

In the first integral, $(\Delta P_t/\alpha)_0$ is conical with respect to the extremity of the leading edge, and the integration over the region of influence can be conveniently made over the two triangles shown in figure 16(a). Considering the differential areas as small triangles, the following equalities are valid:

$$\left. \begin{aligned} dS_4 &= \frac{\lambda^2 c_r^2 f^2}{2} \frac{dg}{(f-g)^2} \\ dS_5 &= \frac{c_r^2 f^2}{2} \frac{dg}{(f+g)^2} \end{aligned} \right\} \quad (A17)$$

Substituting $(\Delta P_t/\alpha)_0$ from equation (A13) and the differential areas from equation (A17) into the first integral of equation (A16) and taking the limits from figure 16(a), gives the result

$$\begin{aligned} \int_{S_t} \left(\frac{\Delta P_t}{\alpha} \right)_0 dS_t &= 2 \int_0^{\frac{f_s}{f c_r - s}} \frac{4f}{\sqrt{f^2 - 1}} \frac{\lambda^2 c_r^2 f^2}{2(f-g)^2} \frac{\cos^{-1}}{\pi} \left(\frac{2gf+g-f}{f+g} \right) dg \\ &+ 2 \int_{\frac{f_s}{f c_r - s}}^1 \frac{4f}{\sqrt{f^2 - 1}} \frac{c_r^2 f^2}{2(f+g)^2} \frac{\cos^{-1}}{\pi} \left(\frac{2gf+g-f}{f+g} \right) dg \end{aligned} \quad (A18)$$

Carrying through the integration yields for the final value of the first integral

$$\int_{S_t} \left(\frac{\Delta P_t}{\alpha} \right)_0 dS_t = \frac{4f^3 \lambda^2 c_r^2}{\pi \sqrt{f^2 - 1}} \left\{ \frac{c_r}{2(fc_r - 2s)} \cos^{-1} \left[\frac{2s(f+1) - fc_r}{fc_r} \right] \right. \\
- \frac{1}{2f} \sqrt{\frac{(f+1)}{(f-1)}} \cos^{-1} \left[\frac{f(c_r - 2s)}{2s - fc_r} \right] - \frac{\pi}{2f} \left[1 - \sqrt{\frac{f(f+1)}{f(f-1)}} \right] \left. \right\} \\
+ \frac{4f^3 c_r^2}{\pi \sqrt{f^2 - 1}} \left\{ \sqrt{\frac{s(fc_r - fs - s)}{f+1}} \left(\frac{1}{f^2 c_r} \right) \right. \\
- \left. \frac{[2s(f+1) - fc_r]}{2f^2 c_r (1+f)} \cos^{-1} \left[\frac{2s(f+1) - fc_r}{fc_r} \right] \right\} \quad (A19)$$

The evaluation of the second integral of equation (A16) can be done conveniently for the two intervals of h shown in figures 16(b) and 16(c). For the interval $s/(c_r - s) \geq h \geq fs/(fc_r - s)$ the region of influence of the infinite triangles on the wing is a single triangle such as S_6 shown in figure 16(b). The differential area is

$$dS_6 = \frac{f^2}{2} \left[\frac{c_r(1+\lambda)}{2} - \frac{s}{h} \right]^2 \frac{dg}{(f-g)^2} \quad (A20)$$

For the interval $1 \geq h \geq s/(c_r - s)$ the region of influence of the infinite triangles on the wing is composed of two triangles such as S_7 and S_8 shown in figure 16(c). The differential areas are

$$\left. \begin{aligned} dS_7 &= \frac{f^2}{2} \left[\frac{c_r(1+\lambda)}{2} - \frac{s}{h} \right]^2 \frac{dg}{(f-g)^2} \\ dS_8 &= \frac{f^2}{2} \left[\frac{c_r(3-\lambda)}{2} - \frac{s}{h} \right]^2 \frac{dg}{(f+g)^2} \end{aligned} \right\} \quad (A21)$$

The second integral of equation (A16) taken over the areas and between the limits shown in figures 16(b) and 16(c) is

$$\iint_{S_t} d\left(\frac{\Delta P_t}{\alpha}\right) dS_t = 2 \int_{\frac{f_s}{f c_r - s}}^{\frac{s}{c_r - s}} \int_0^1 \frac{8hf}{\pi^2 \sqrt{1-h^2} (f^2 - h^2)} \frac{f^2}{2} \left[\frac{c_r(1+\lambda)}{2} - \frac{s}{h} \right]^2 \cos^{-1} \left[\frac{2gh+g-h}{g+h} \right] \frac{dh dg}{(f-g)^2}$$

$$+ 2 \int_{\frac{s}{c_r - s}}^1 \int_0^{\frac{hs}{hc_r - s}} \frac{8hf}{\pi^2 \sqrt{1-h^2} (f^2 - h^2)} \frac{f^2}{2} \left[\frac{c_r(1+\lambda)}{2} - \frac{s}{h} \right]^2 \cos^{-1} \left(\frac{2gh+g-h}{g+h} \right) \frac{dh dg}{(f-g)^2}$$

$$+ 2 \int_{\frac{s}{c_r - s}}^1 \int_{\frac{hs}{hc_r - s}}^1 \frac{8hf}{\pi^2 \sqrt{1-h^2} (f^2 - h^2)} \frac{f^2}{2} \left[\frac{c_r(3-\lambda)}{2} - \frac{s}{h} \right]^2 \cos^{-1} \left(\frac{2gh+g-h}{g+h} \right) \frac{dh dg}{(f+g)^2}$$

(A22)

Performing the integration with respect to g and substituting the limits gives the result

NACA RM No. A8E06

$$\begin{aligned}
 \iint_{S_t} d\left(\frac{\Delta P_t}{\alpha}\right) dS_t &= 2 \int_{\frac{f s}{f c_r - s}}^{\frac{s}{c_r - s}} \frac{8 h f}{\pi^2 \sqrt{1-h^2} (f^2 - h^2)} \left(\frac{f^2}{2}\right) \left[\frac{c_r(1+\lambda)}{2} - \frac{s}{h}\right]^2 \left\{ \frac{\pi}{h+f} \left[\sqrt{\frac{h(h+1)}{f(f-1)}} - \frac{h}{f} \right] \right\} dh \\
 &+ 2 \int_{\frac{s}{c_r - s}}^1 \frac{8 h f}{\pi^2 \sqrt{1-h^2} (f^2 - h^2)} \frac{f^2}{2} \left[\frac{c_r(1+\lambda)}{2} - \frac{s}{h}\right]^2 \left\{ \frac{h^2 c_r}{(h+f)[f(h c_r - s) - h s]} \cos^{-1} \left[\frac{2s(h+1) - h c_r}{h c_r} \right] \right. \\
 &- \left. \sqrt{\frac{h(h+1)}{f(f-1)}} \frac{1}{h+f} \cos^{-1} \left[\frac{2hs(1-f)}{hs - (h c_r - s)f} - 1 \right] - \left(\frac{\pi}{h+f} \right) \left[\frac{h}{f} - \sqrt{\frac{h(h+1)}{f(f-1)}} \right] \right\} dh \\
 &+ 2 \int_{\frac{s}{c_r - s}}^1 \frac{8 h f}{\pi^2 \sqrt{1-h^2}} \frac{1}{(f^2 - h^2)} \frac{f^2}{2} \left[\frac{c_r(3-\lambda)}{2} - \frac{s}{h}\right]^2 \left\{ \frac{-h^2 c_r}{f(h c_r - s) + h s} \left(\frac{1}{f-h}\right) \cos^{-1} \left[\frac{2s(h+1) - h c_r}{h c_r} \right] \right. \\
 &- \left. \sqrt{\frac{h(h+1)}{f(f+1)}} \frac{1}{(h-f)} \cos^{-1} \left[\frac{2hs(f+1)}{hs + f(h c_r - s)} - 1 \right] \right\} dh
 \end{aligned}
 \tag{A23}$$

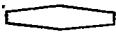



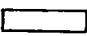


The actual integration of (A23) was done graphically in the present case because an analytical integration would be very difficult and because the contribution of equation (A23) to the lift-curve slope is very small.

To summarize the procedure to obtain the lift-curve slope, the value of the first three integrals in equation (A1) are obtained from equations (A8), (A10), and (A12), respectively. The negative contribution of the tips given by the fourth integral in equation (A1) is obtained by subtracting the result of equation (A23) from the result of equation (A19) in accordance with equation (A16). For the present wing, the value of the fourth integral was 39 percent of the value of the sum of the first three integrals, illustrating the very appreciable effect of the tips in reducing the lift-curve slope.

REFERENCES

1. Vincenti, Walter G., Nielsen, Jack N., and Matteson, Frederick H.: Investigation of Wing Characteristics at a Mach Number of 1.53. I - Triangular Wings of Aspect Ratio 2. NACA RM No. A7I10, 1947.
2. Vincenti, Walter G., Van Dyke, Milton D., and Matteson, Frederick H.: Investigation of Wing Characteristics at a Mach Number of 1.53. II - Swept Wings of Taper Ratio 0.5. NACA RM No. A8EO5, 1948.
3. Nielsen, Jack N.: Effect of Aspect Ratio and Taper on the Pressure Drag at Supersonic Speeds of Unswept Wings at Zero Lift. NACA TN No. 1487, 1947.
4. Lagerstrom, P. A., and Wall, D.: Formulas in Three-Dimensional Wing Theory. (1) Douglas Aircraft Co. Rep. No. SM 11901, July 8, 1946.
5. Ferri, Antonio: Experimental Results with Airfoils Tested in the High-Speed Tunnel at Guidonia. NACA TM No. 946, 1940.
6. Cohen, Doris: The Theoretical Lift of Flat Swept-Back Wings at Supersonic Speeds. NACA TN No. 1555, 1948.
7. Jones, Robert T.: Thin Oblique Airfoils at Supersonic Speed. NACA TN No. 1107, 1946.

TABLE I.— SUMMARY OF GEOMETRIC PROPERTIES OF WINGS

Wing	U-1	U-2	U-3	U-4	U-5	U-6	U-7
Sketch							
Λ_o (deg)	6.34	9.46	18.44	33.69	0	18.44	26.57
Λ_1 (deg)	-6.34	-9.46	-18.44	-33.69	0	-18.44	-26.57
A	6.000	4.000	2.000	1.000	4.000	4.000	4.000
c_t/c_r	0.5	0.5	0.5	0.5	1.0	0.2	0
b (in.)	7.348	6.000	4.242	3.000	6.000	6.000	6.000
\bar{c}_g (in.)	1.224	1.500	2.121	3.000	1.500	1.500	1.500
\bar{c}_a (in.)	1.269	1.556	2.200	3.111	1.500	1.722	2.000
x_o (in.)	0.816	1.000	1.414	2.000	0.750	1.250	1.500
c_r (in.)	1.632	2.000	2.828	4.000	1.500	2.500	3.000





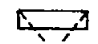





Properties common to all wings:

$$S = 9 \text{ sq in.}$$

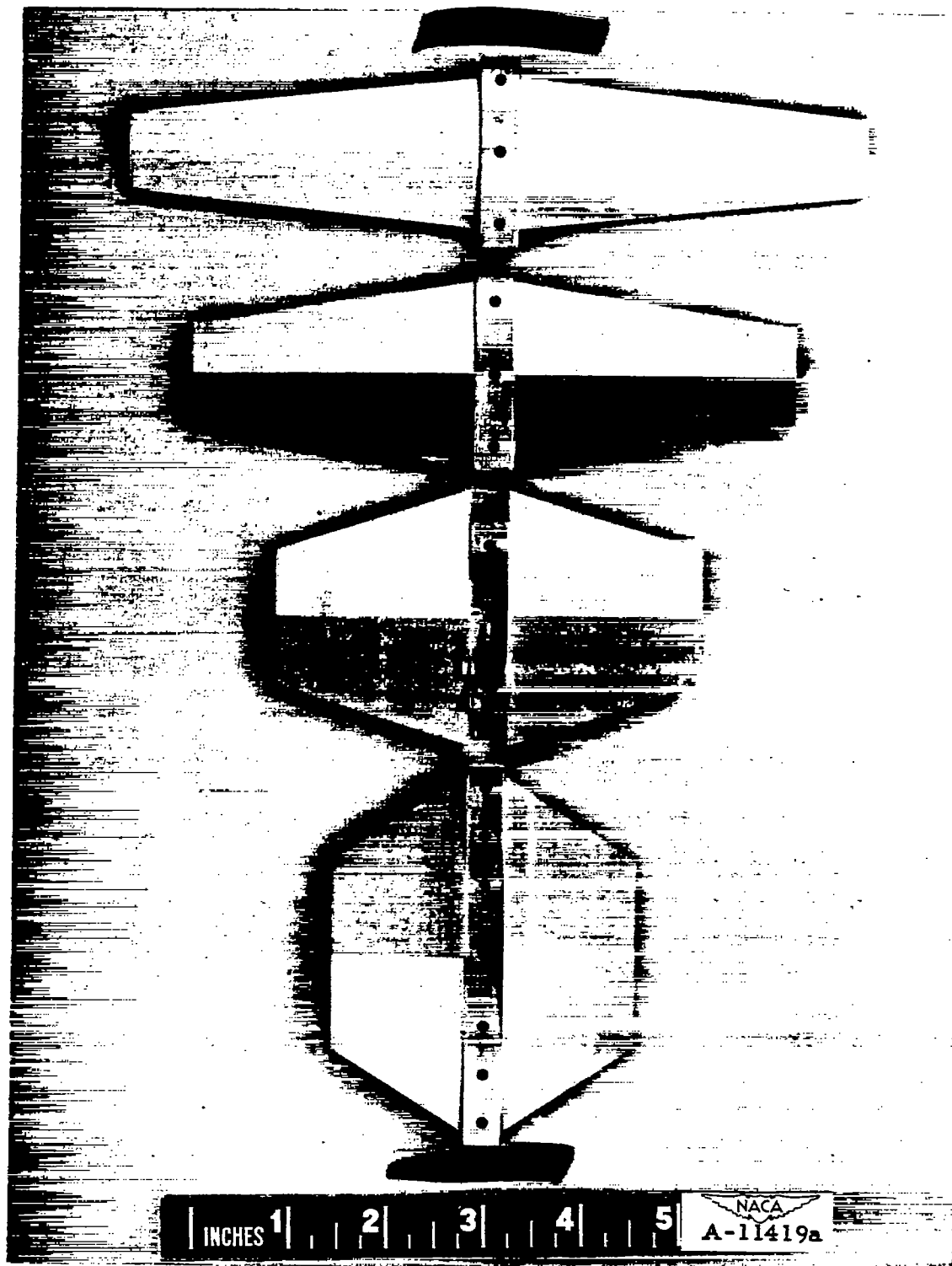
$$\frac{\Lambda_1}{2} = 0^\circ$$

TABLE II.- SUMMARY OF RESULTS OF FIGURE 3

Wing	Sketch	Lift		Moment		Drag				Lift-drag ratio	
		$\alpha_{L=0}$ [deg]	$\left(\frac{dC_L}{d\alpha}\right)_{L=0}$ [per deg]	$C_{m_{L=0}}$	$\left(\frac{dC_m}{dC_L}\right)_{av}$	C_{Dmin}	$C_{L_{D=min}}$	$\Delta C_D/(\Delta C_L)^2$	k_a	$(L/D)_{max}$	$C_{L_{opt}}$
U-1		0.5 (-.07)	0.0575 (.0579)	-0.034 (-.044)	0.056 (.007)	0.0241 (.0174)	0.03 (0)	0.320 (.302)	1.09 (1.00)	6.1 (6.9)	0.28 (.24)
U-2		.4 (-.12)	.0560 (.0562)	-.033 (-.044)	.064 (.012)	.0240 (.0175)	.02 (0)	.315 (.310)	1.07 (1.00)	6.1 (6.8)	.29 (.24)
U-3		.1 (-.38)	.0500 (.0500)	-.040 (-.047)	.114 (.039)	.0222 (.0178)	.03 (0)	.358 (.349)	1.05 (1.00)	6.2 (6.3)	.25 (.23)
U-4		-.5 (-1.36)	.0360 (.0337)	-.042 (*)	.200 (*)	.0210 (.0174)	.04 (0)	.517 (.517)	1.09 (1.00)	5.6 (5.3)	.20 (.18)
U-5		.3 (-.17)	.0570 (.0538)	-.033 (-.043)	.079 (.020)	.0245 (.0172)	.02 (0)	.310 (.324)	1.03 (1.00)	6.0 (6.7)	.29 (.23)
U-6		.5 (-.11)	.0565 (.0576)	-.039 (-.045)	.078 (.013)	.0242 (.0178)	.03 (0)	.300 (.303)	1.01 (1.00)	6.4 (6.8)	.29 (.24)
U-7		.4 (-.15)	.0560 (.0572)	-.037 (-.047)	.052 (.020)	.0235 (.0181)	.03 (0)	.323 (.305)	1.07 (1.00)	6.3 (6.7)	.27 (.24)
Linear	Section 	0	.0603	-.043	0	.0173	0	.289	1.00	7.1	.24
Second-order		.36	.0603	-.043	.032	.0170	.011	.289	1.00	7.5	.24
Shock-exp.	Theory	.37	.0615	-.043	.034	.0172	.014	.300	1.00	7.4	.26

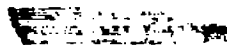
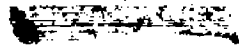
Note: For each wing the experimental value is given first and the corresponding theoretical value indicated in parentheses directly below. Where an asterisk is used, the theoretical value has not been computed. The theoretical values for all quantities in the table pertaining to drag and lift-drag ratio include the pressure drag only.

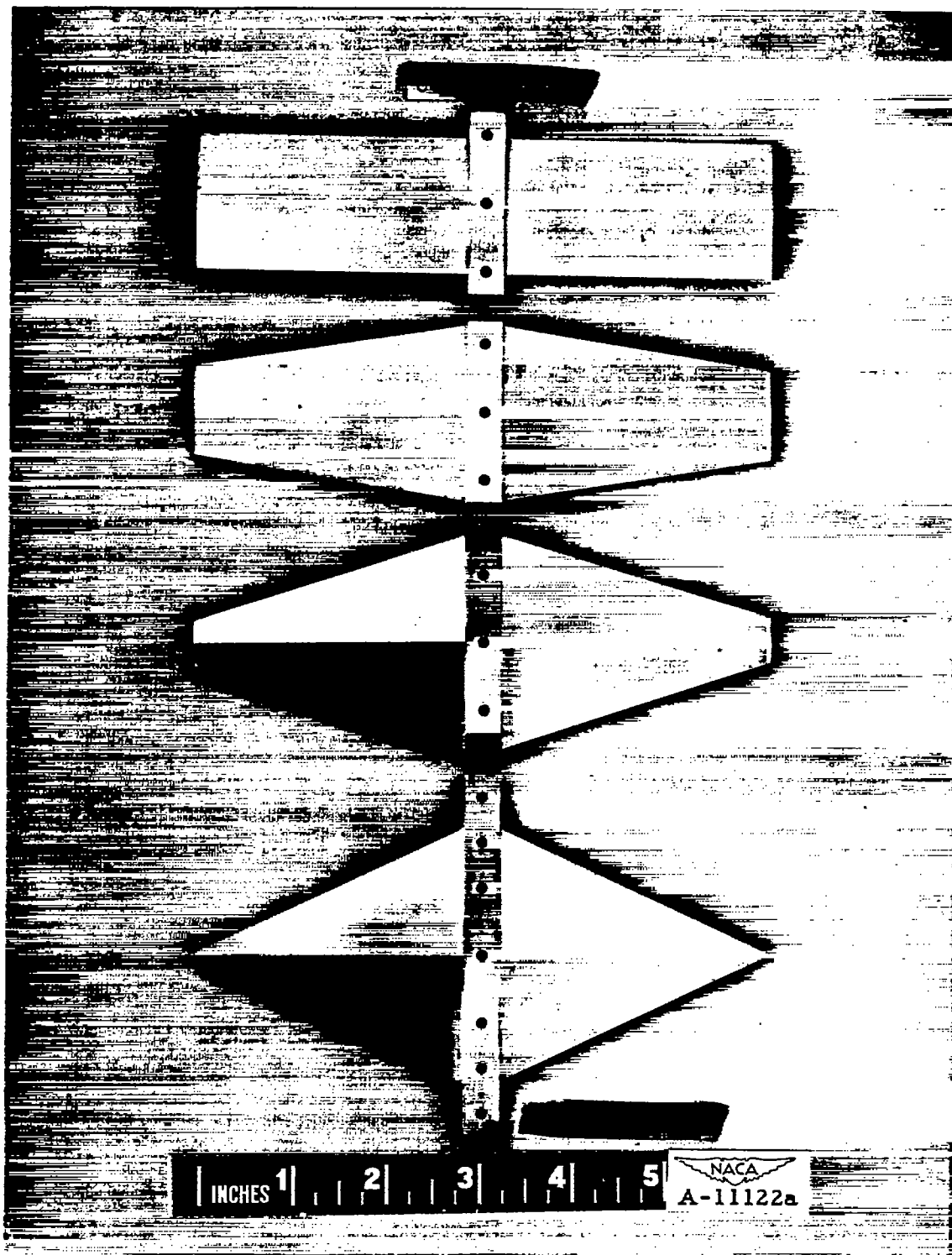
NACA



(a) Aspect-ratio series.

Figure 1.— Models.



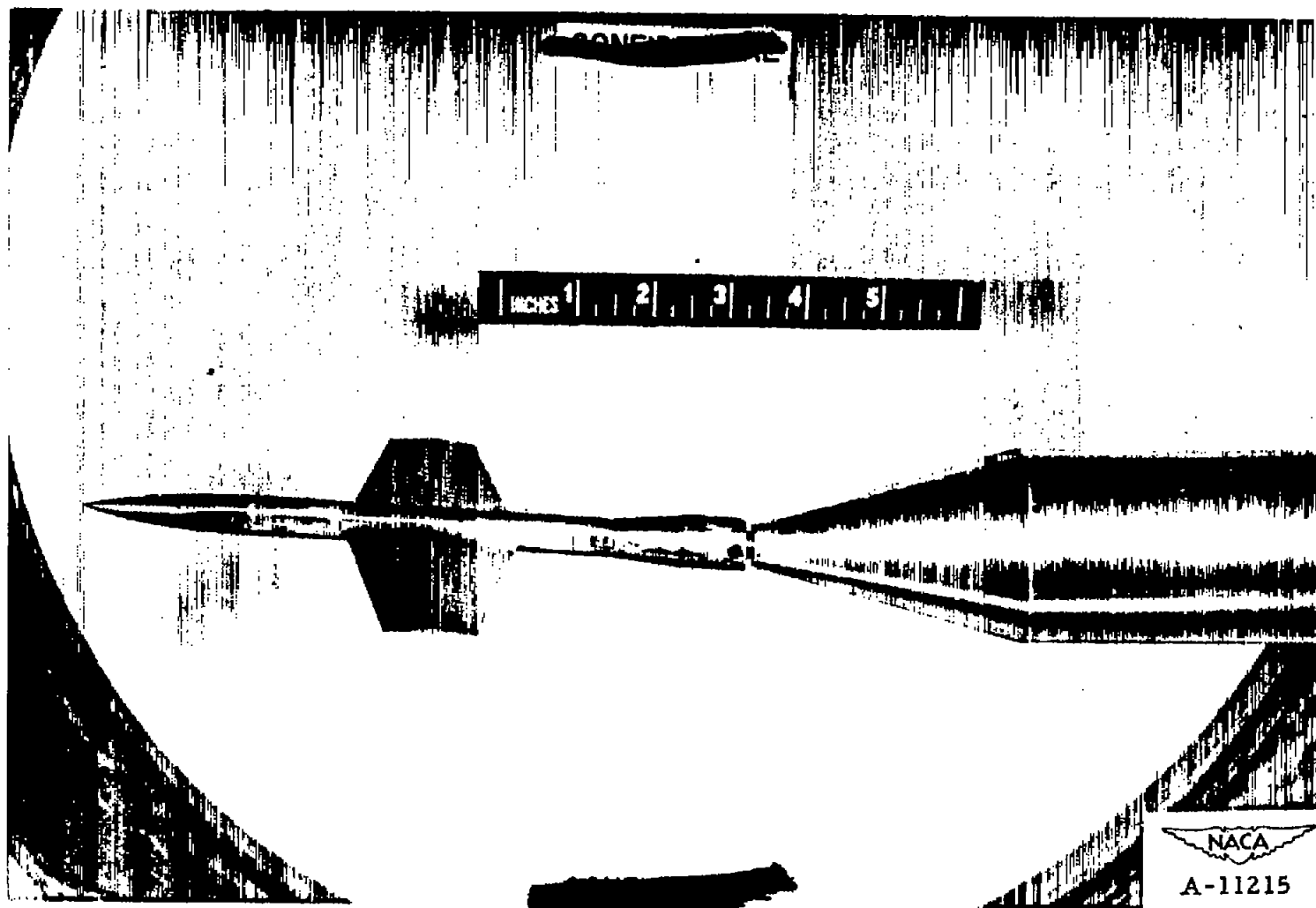


(b) Taper-ratio series.

Figure 1.- Continued.

RECEIVED

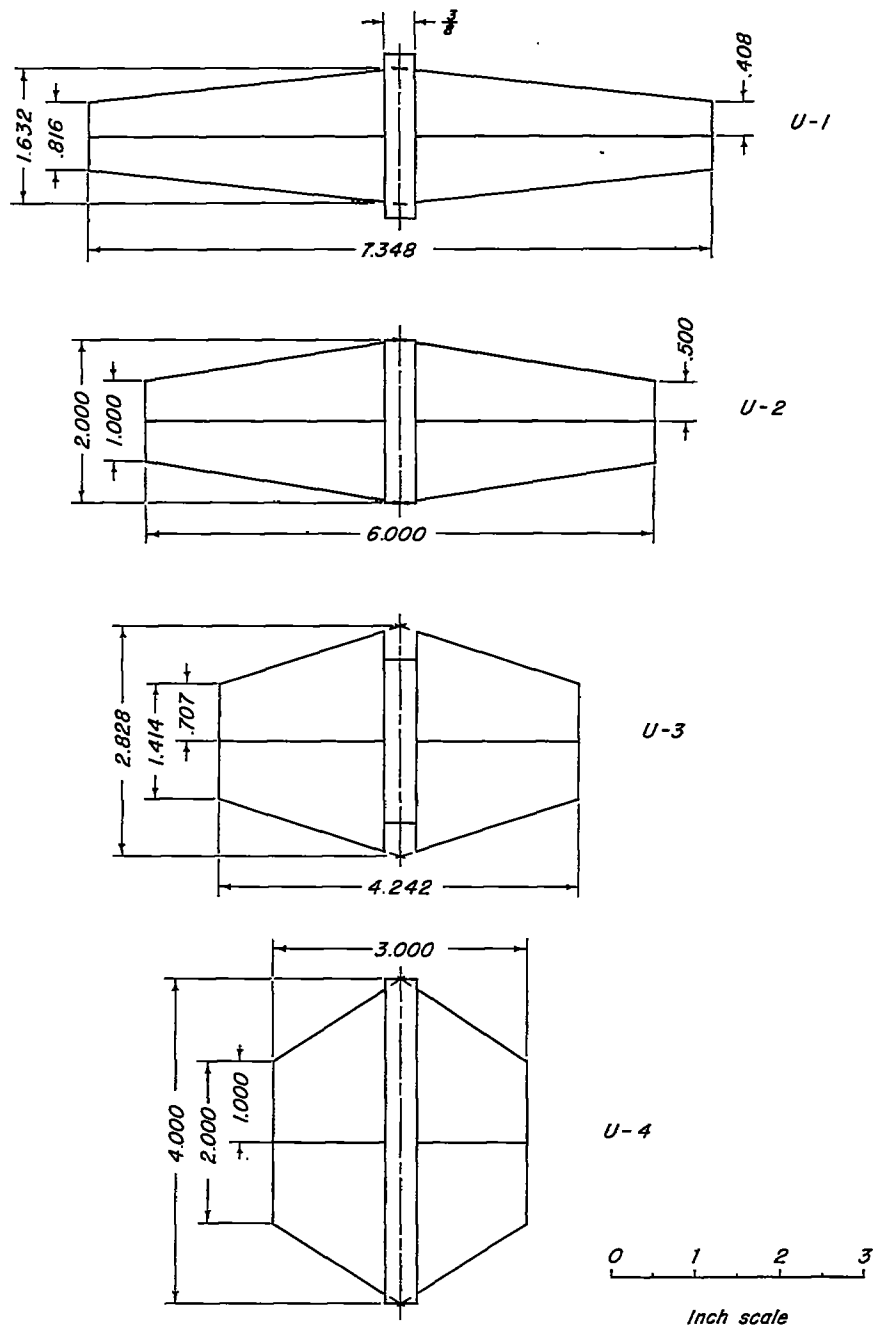
RECEIVED



(c) Model mounted in tunnel.

Figure 1.— Concluded.



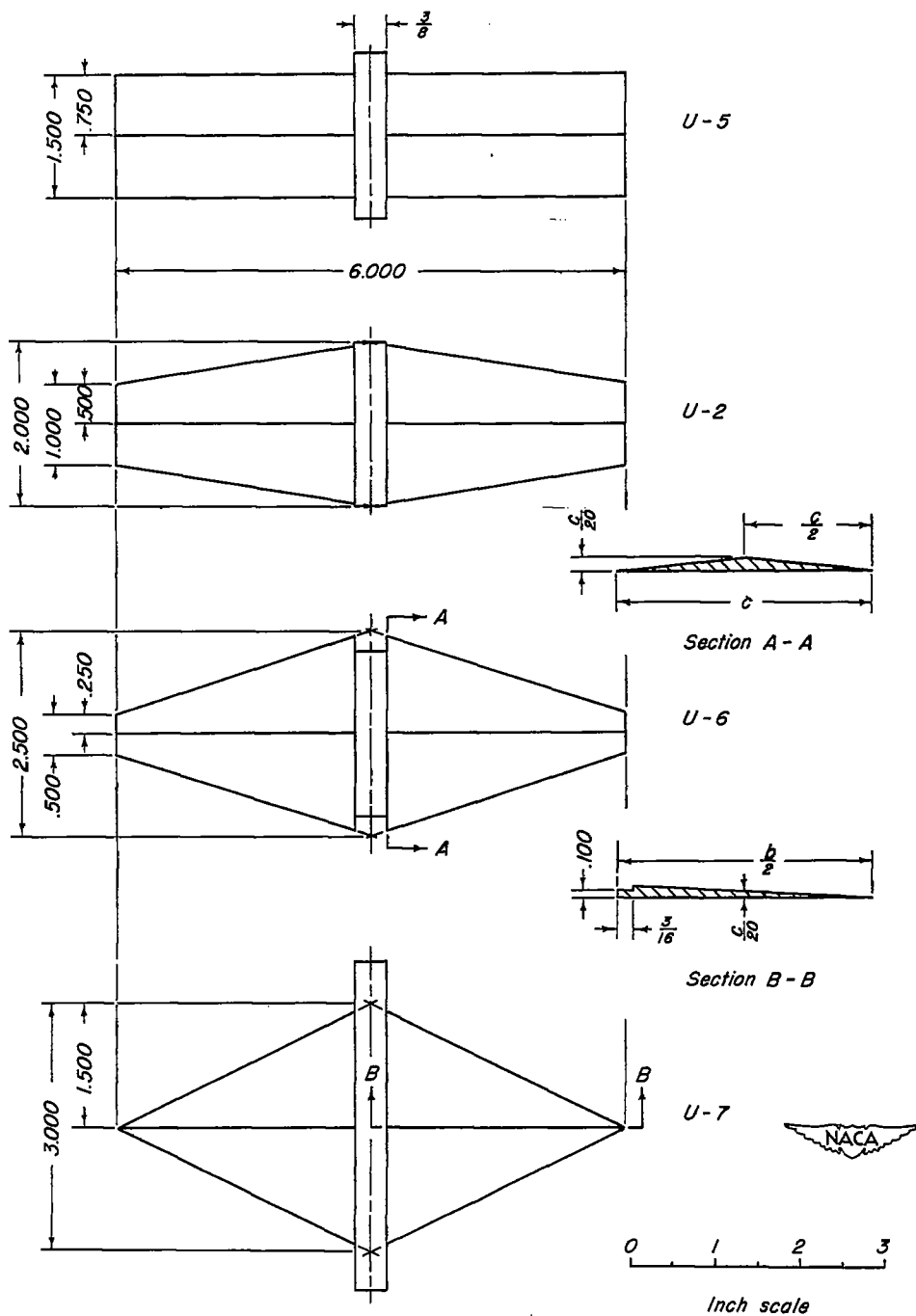


(a) Aspect-ratio series.

Figure 2. - Dimensions of models.

~~CONFIDENTIAL~~

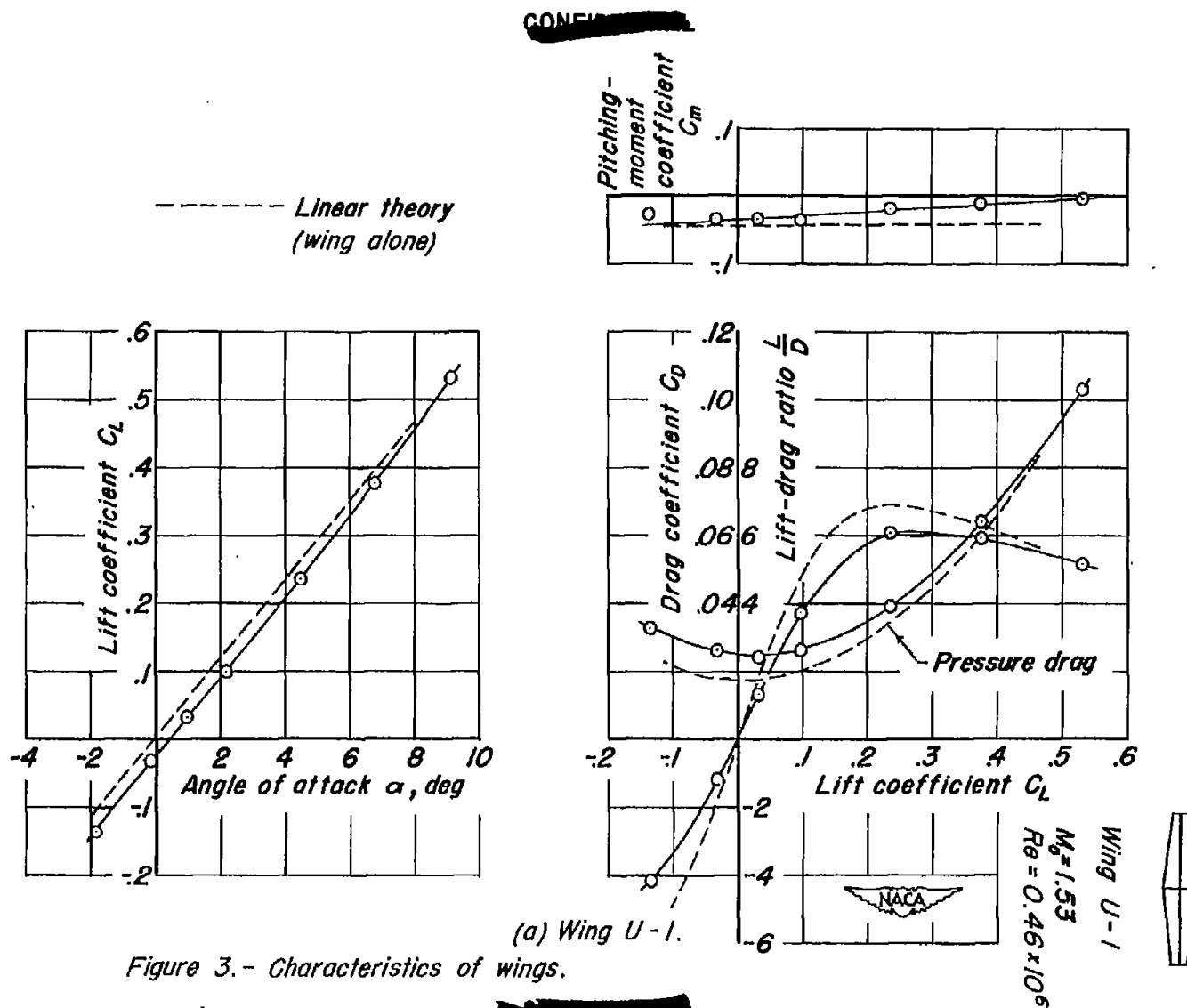
NACA RM No. A8E06



(b) Taper - ratio series.

Figure 2. - Concluded.

~~CONFIDENTIAL~~



CONFIDENTIAL

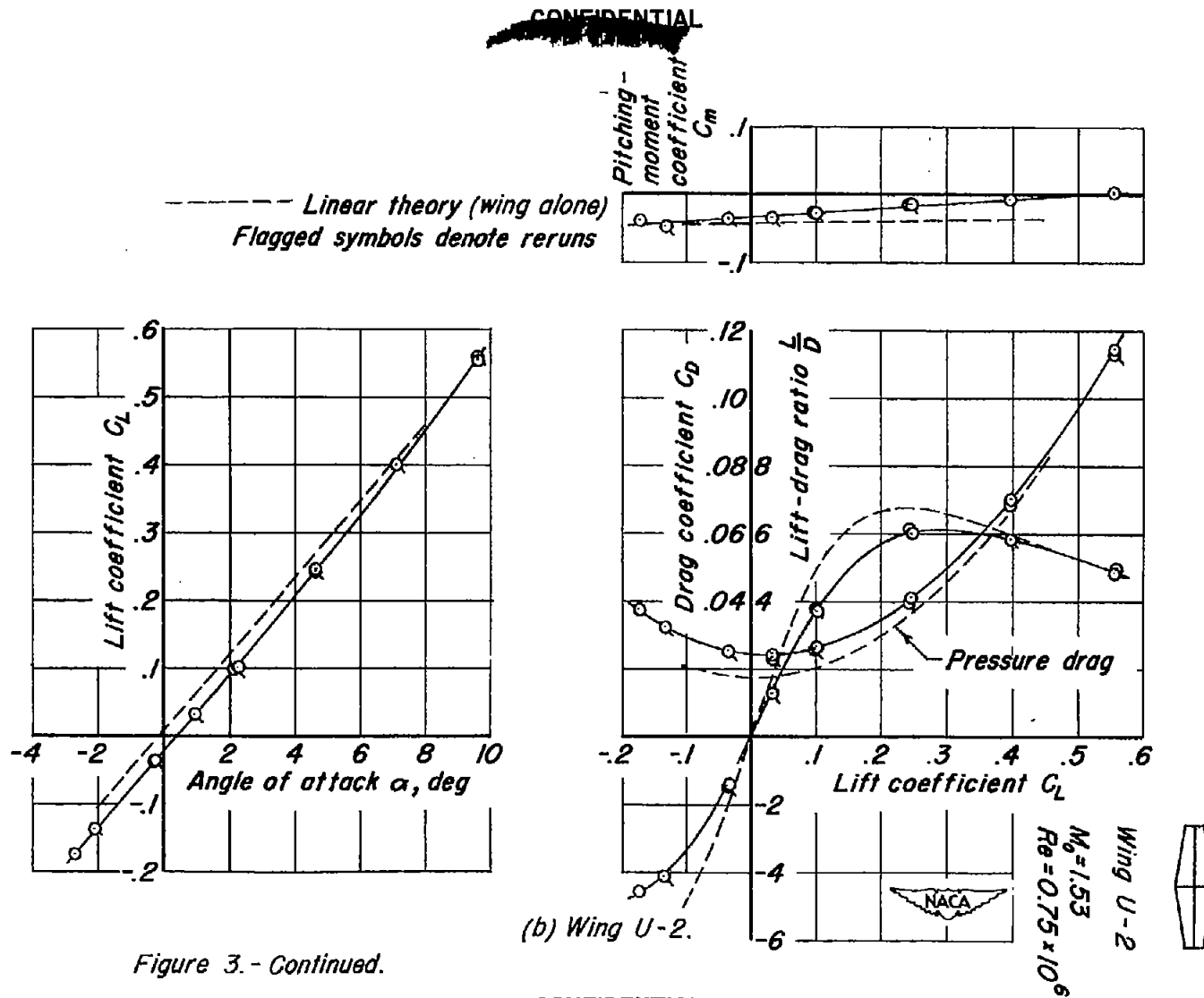


Figure 3. - Continued.

CONFIDENTIAL

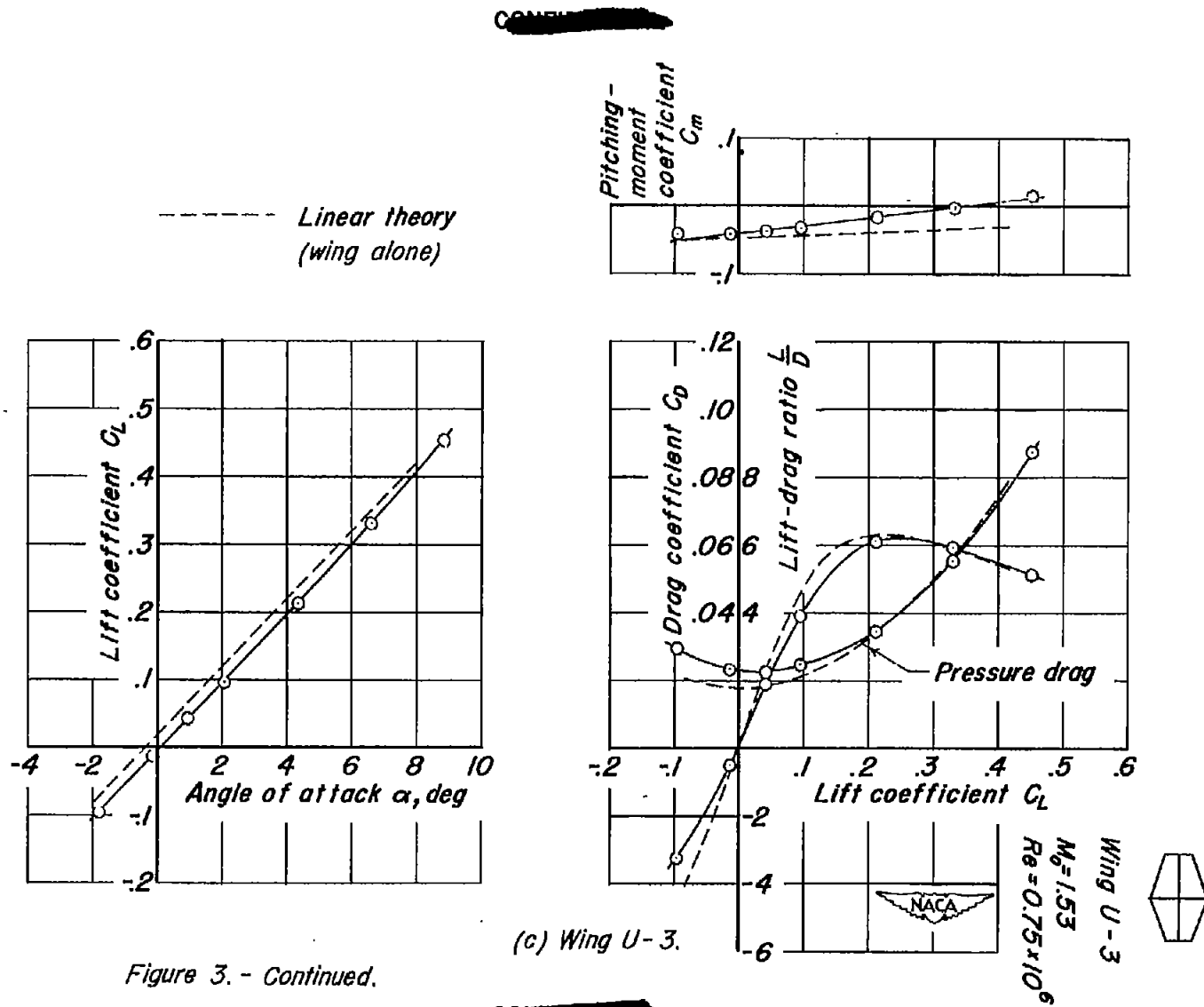


Figure 3. - Continued.

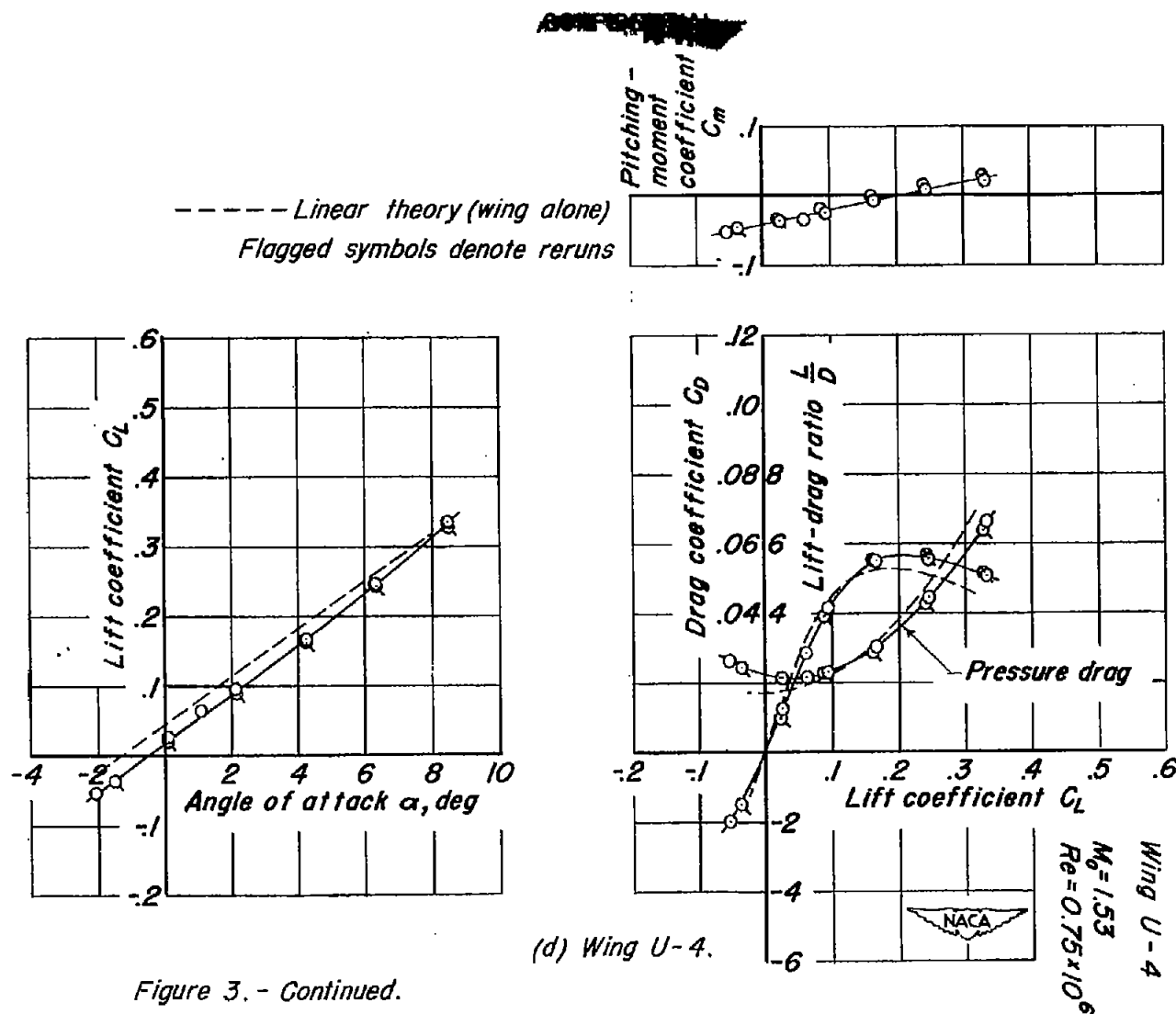


Figure 3. - Continued.

(d) Wing U-4.

~~CONFIDENTIAL~~

CONFIDENTIAL

NACA RM No. A8106

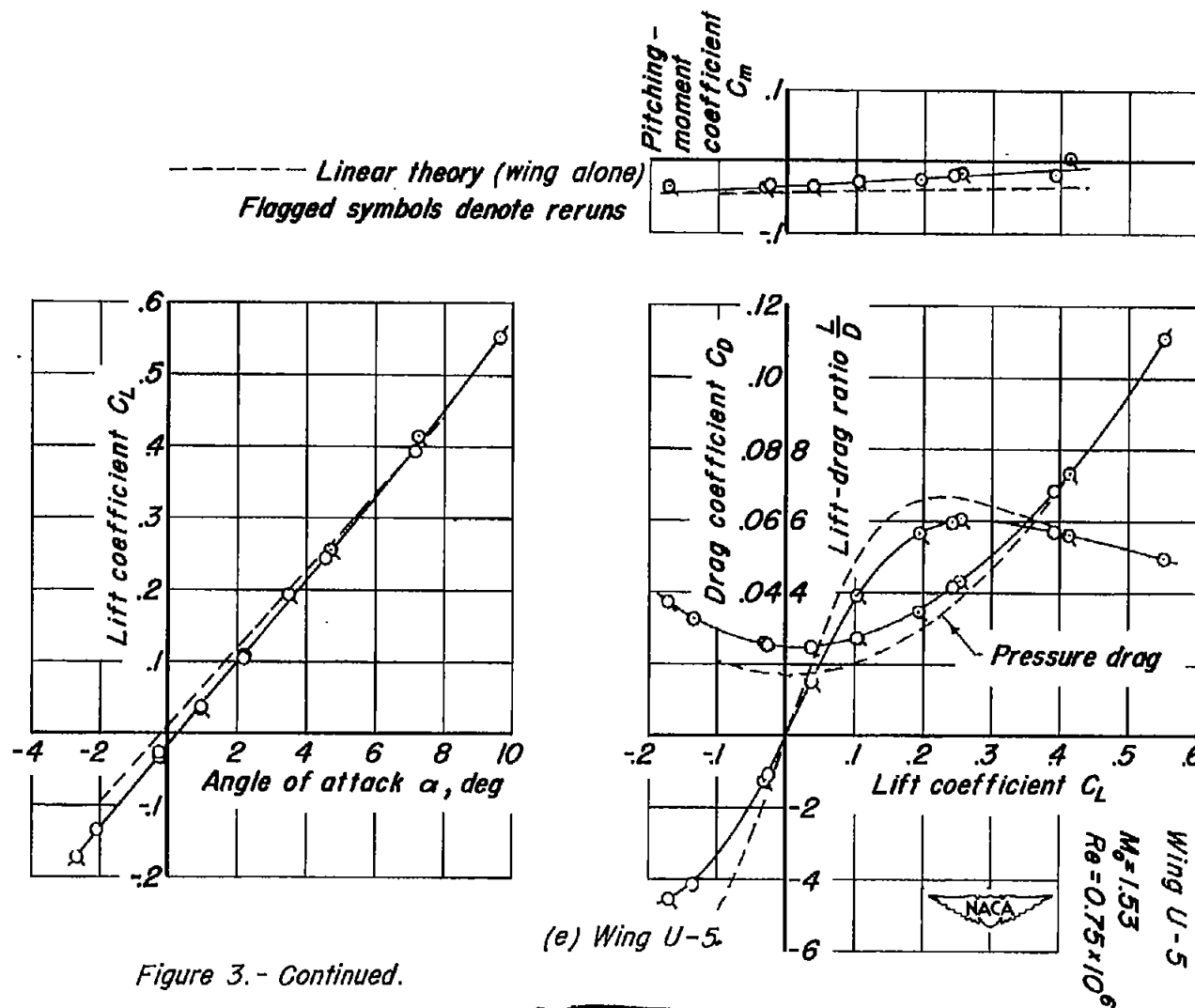


Figure 3.- Continued.

CONFIDENTIAL

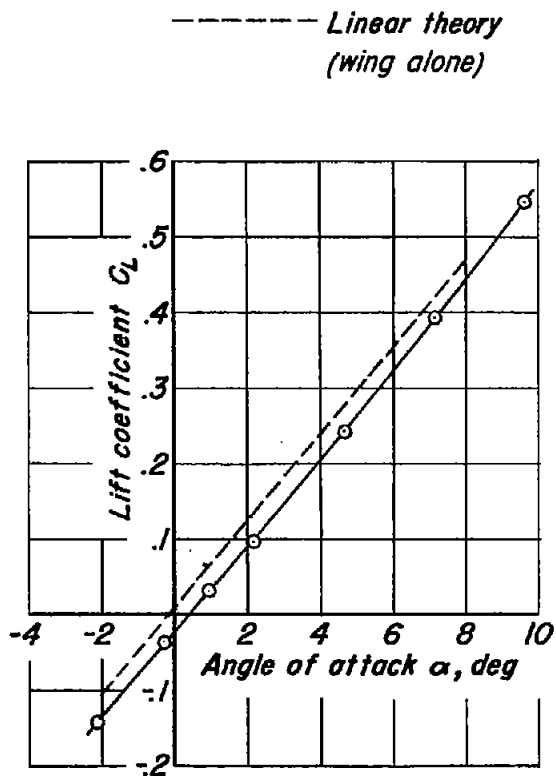
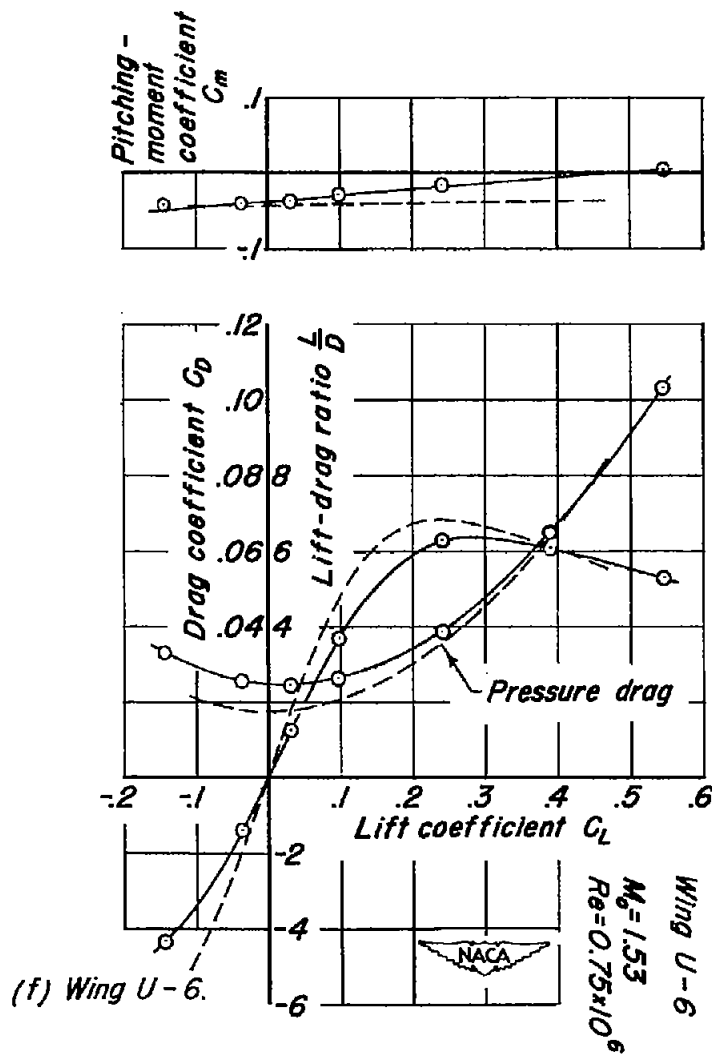


Figure 3.- Continued.



CONFIDENTIAL

~~CONFIDENTIAL~~

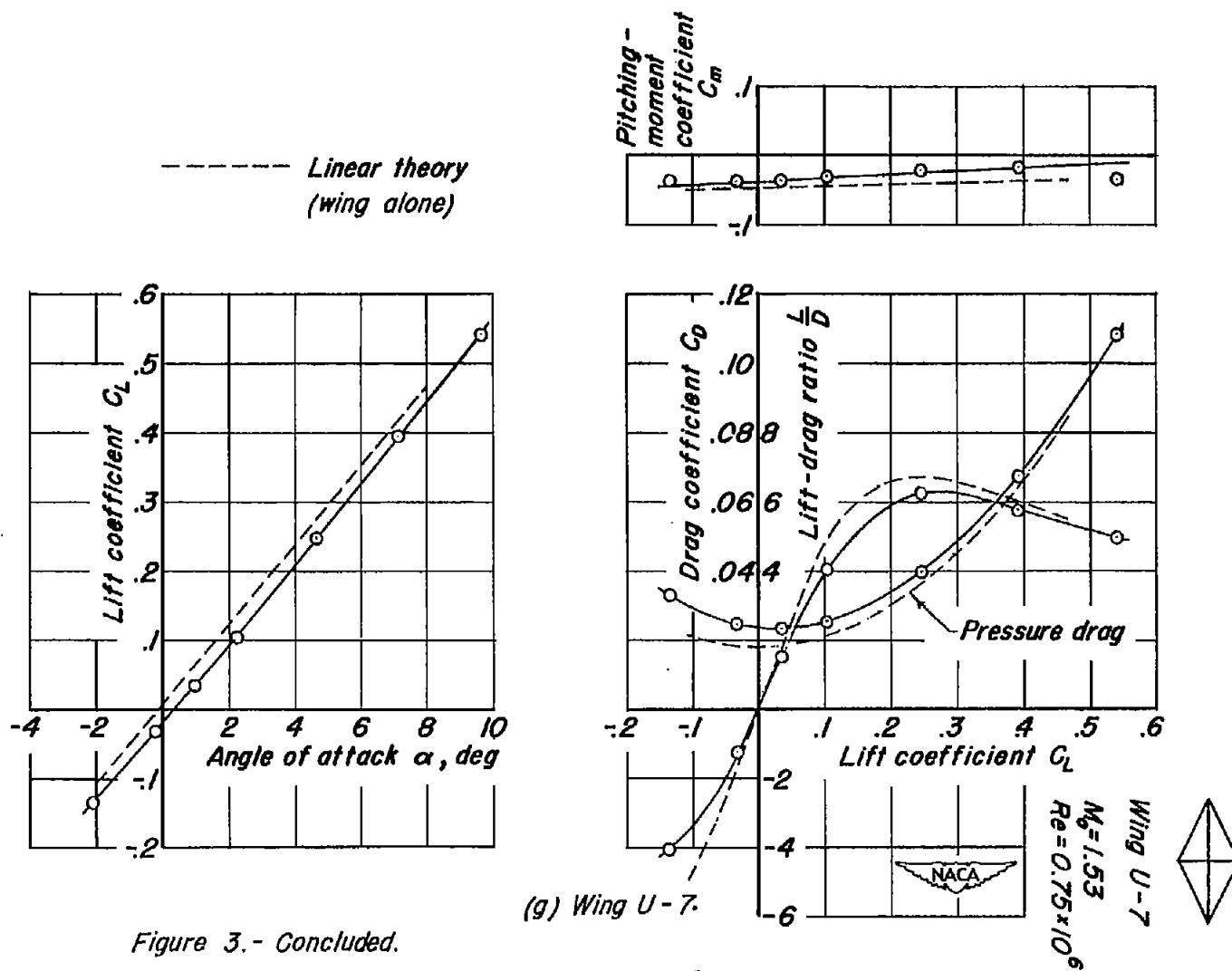


Figure 3.- Concluded.

(g) Wing U-7.

~~CONFIDENTIAL~~

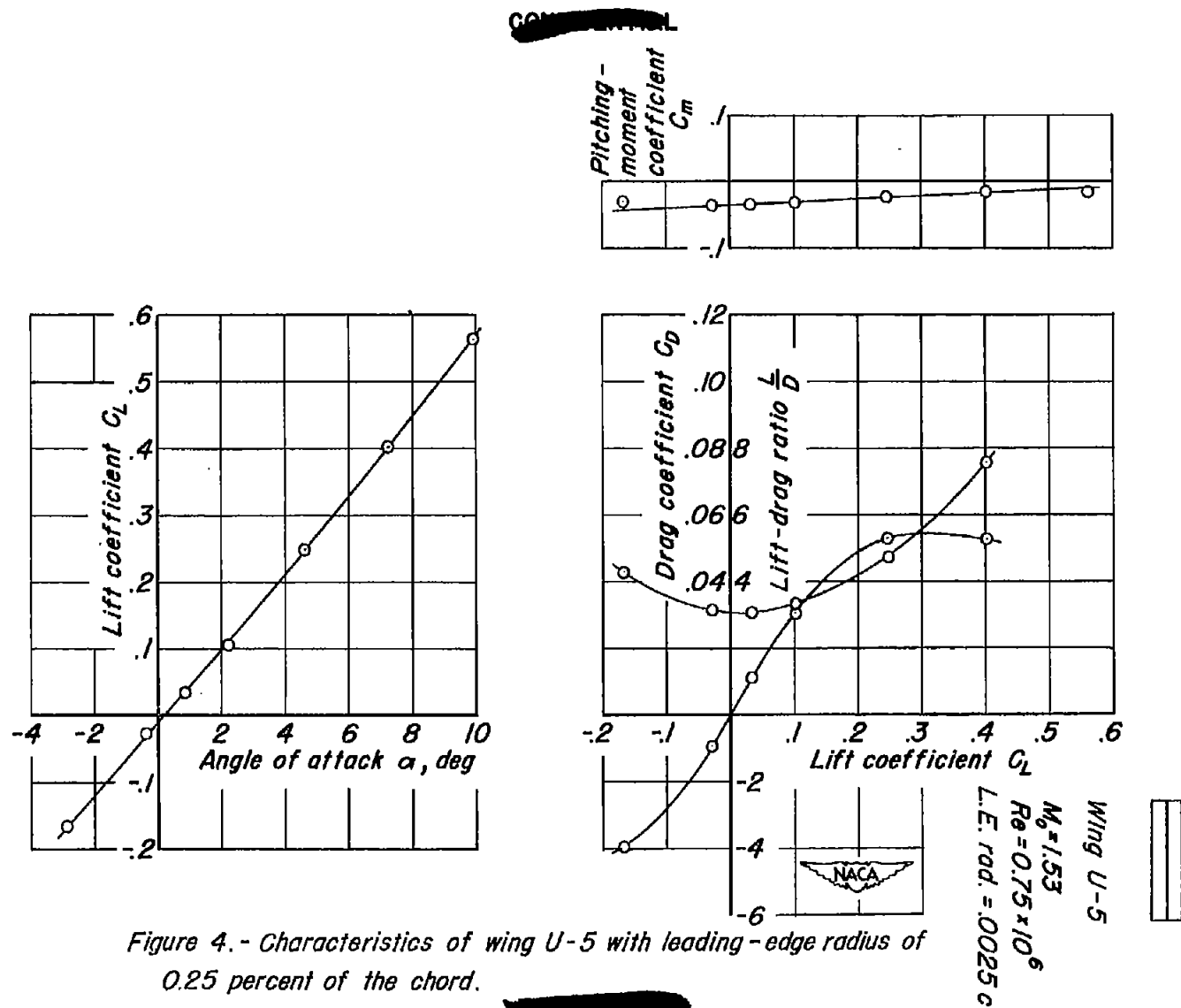
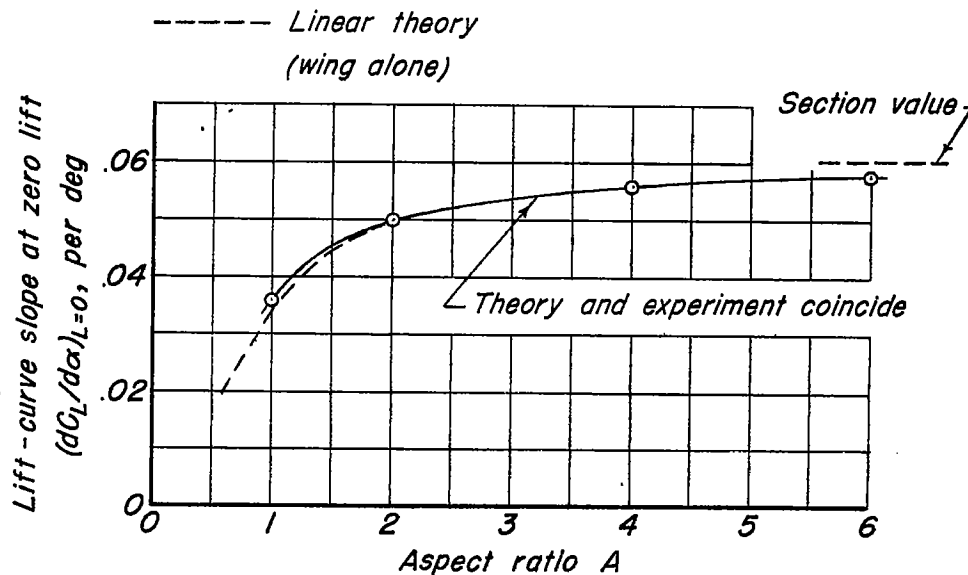
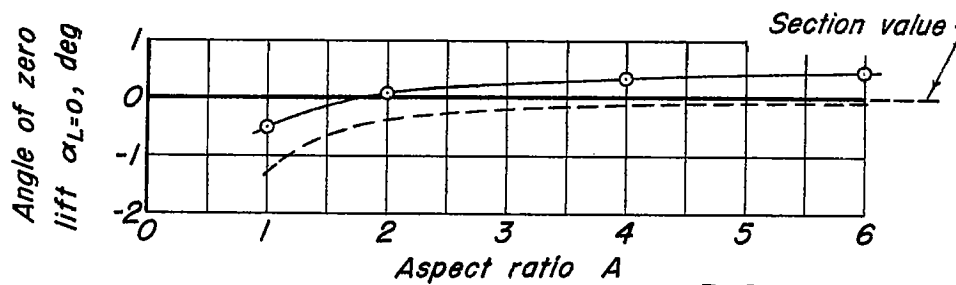


Figure 4. - Characteristics of wing U-5 with leading-edge radius of 0.25 percent of the chord.

$M_o = 1.53$



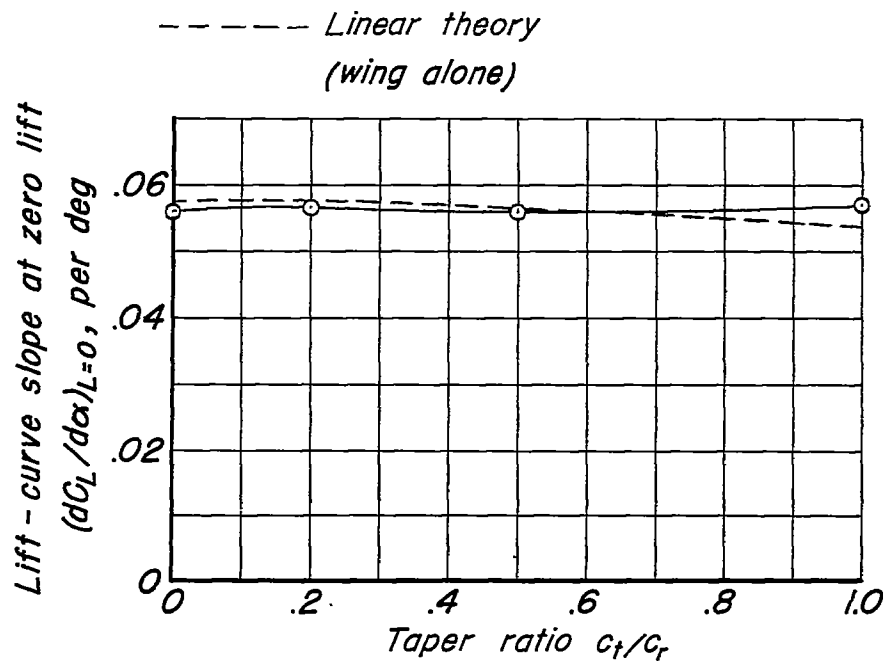
(a) Lift - curve slope.



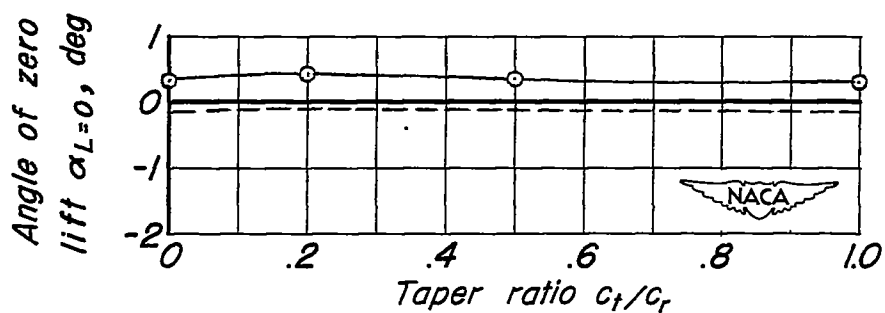
(b) Angle of zero lift.

Figure 5.- Lift characteristics of aspect - ratio series.

$$M_o = 1.53$$



(a) Lift - curve slope.

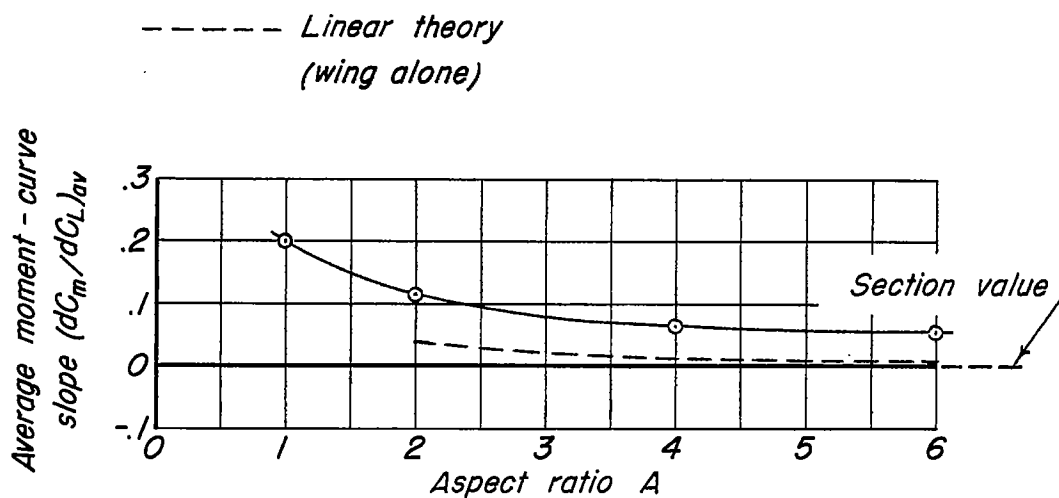


(b) Angle of zero lift.

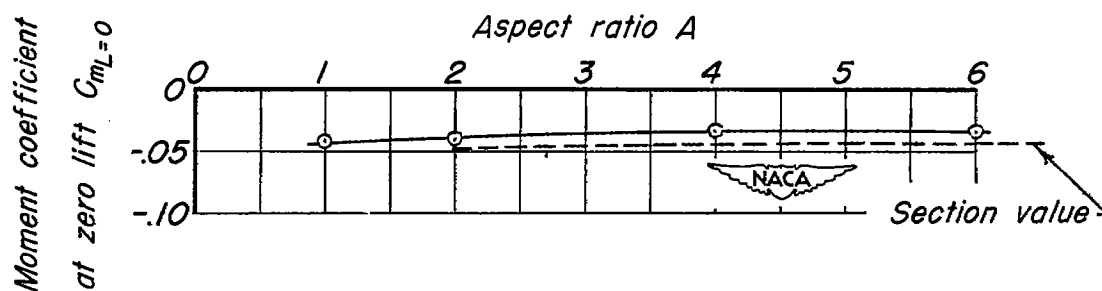
Figure 6. - Lift characteristics of taper - ratio series.

~~CONFIDENTIAL~~

$$M_o = 1.53$$



(a) Average moment - curve slope.



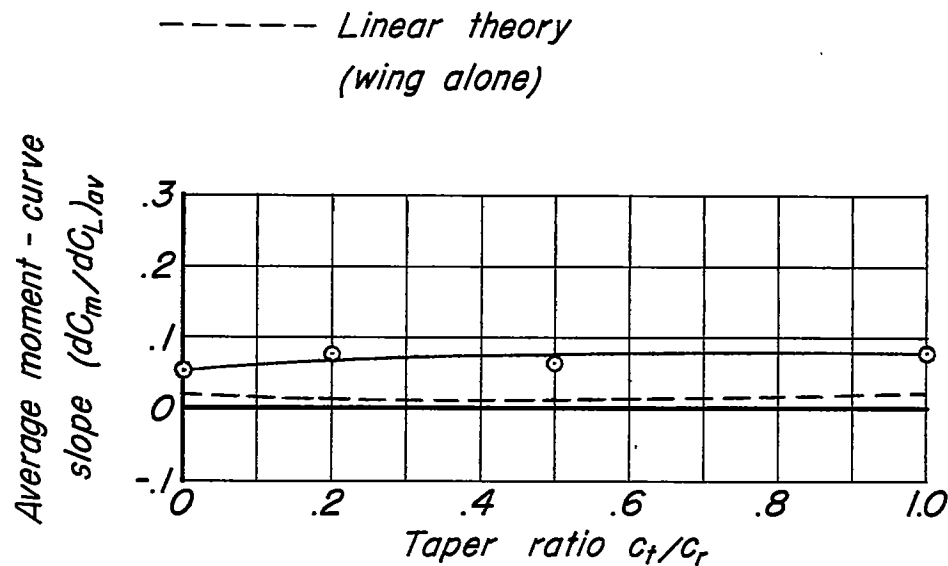
(b) Moment coefficient at zero lift.

Figure 7. - Moment characteristics of aspect - ratio series.

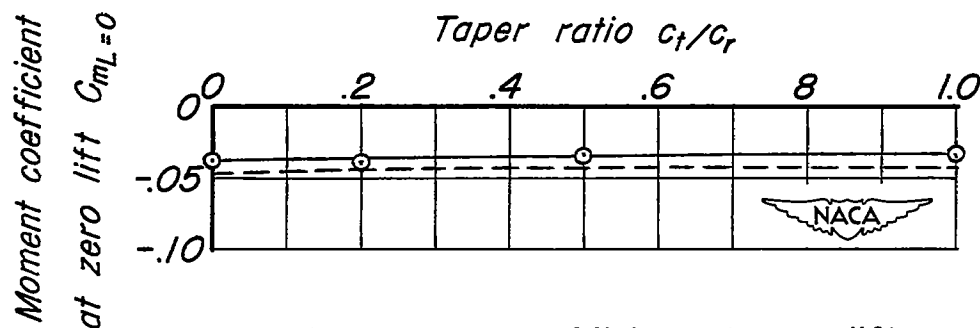
~~CONFIDENTIAL~~

CONFIDENTIAL

$$M_0 = 1.53$$



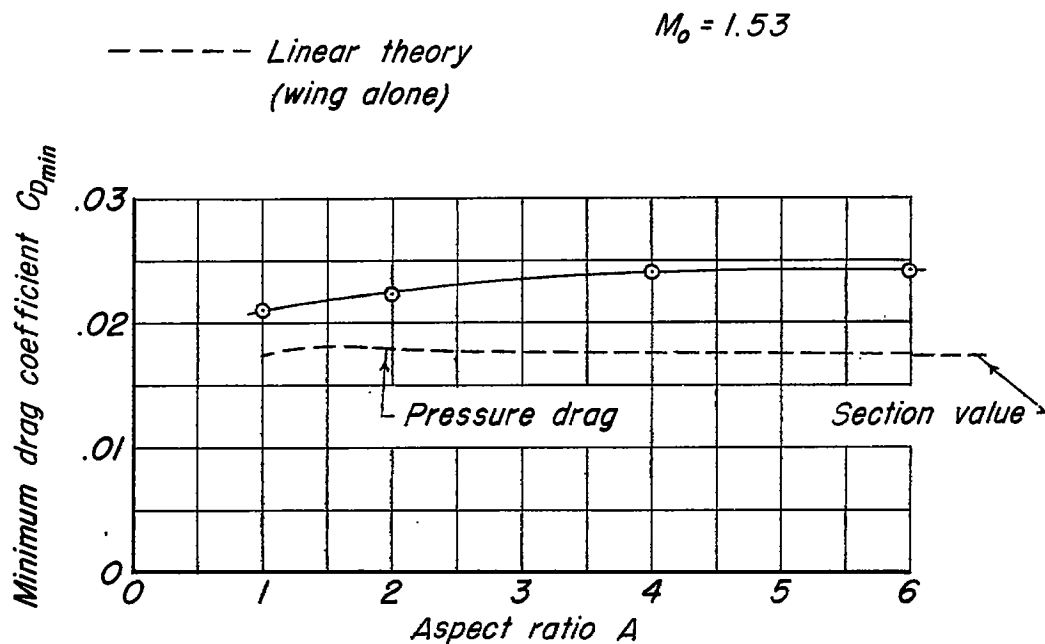
(a) Average moment - curve slope.



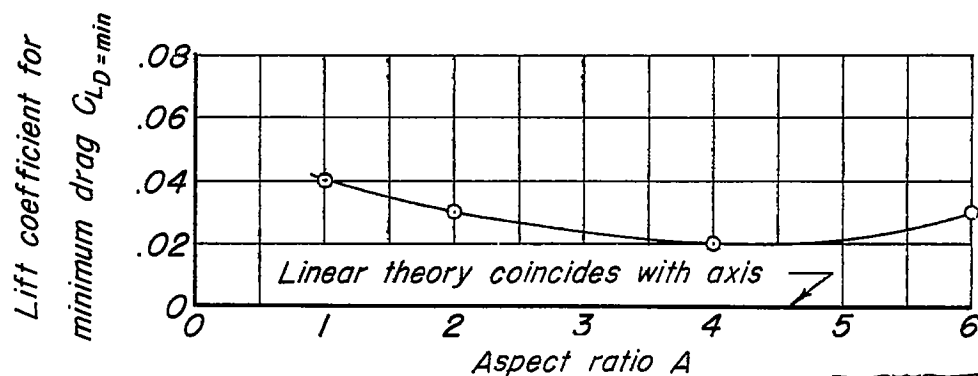
(b) Moment coefficient at zero lift.

Figure 8.- Moment characteristics of taper - ratio series.

CONFIDENTIAL



(a) Minimum drag coefficient.



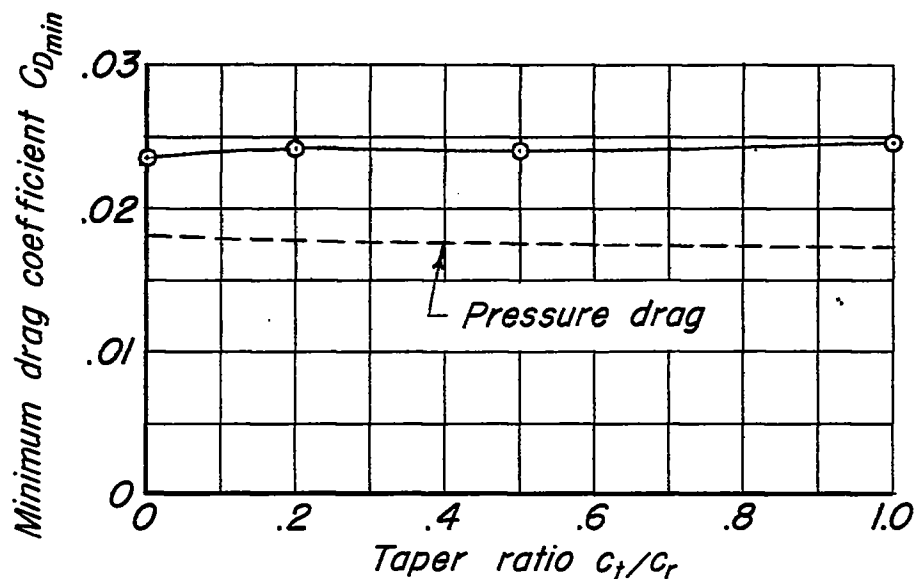
(b) Lift coefficient for minimum drag.

Figure 9.- Minimum-drag characteristics of aspect-ratio series.

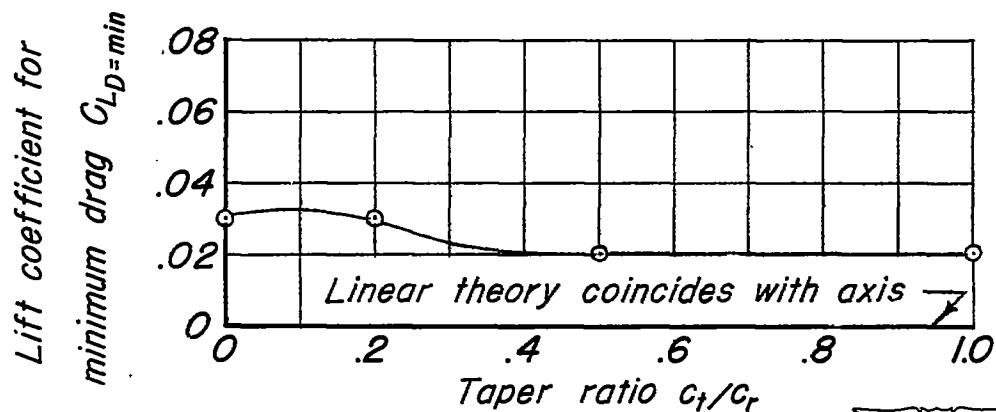
~~CONFIDENTIAL~~

$M_0 = 1.53$

----- Linear theory
 (wing alone)



(a) Minimum drag coefficient.

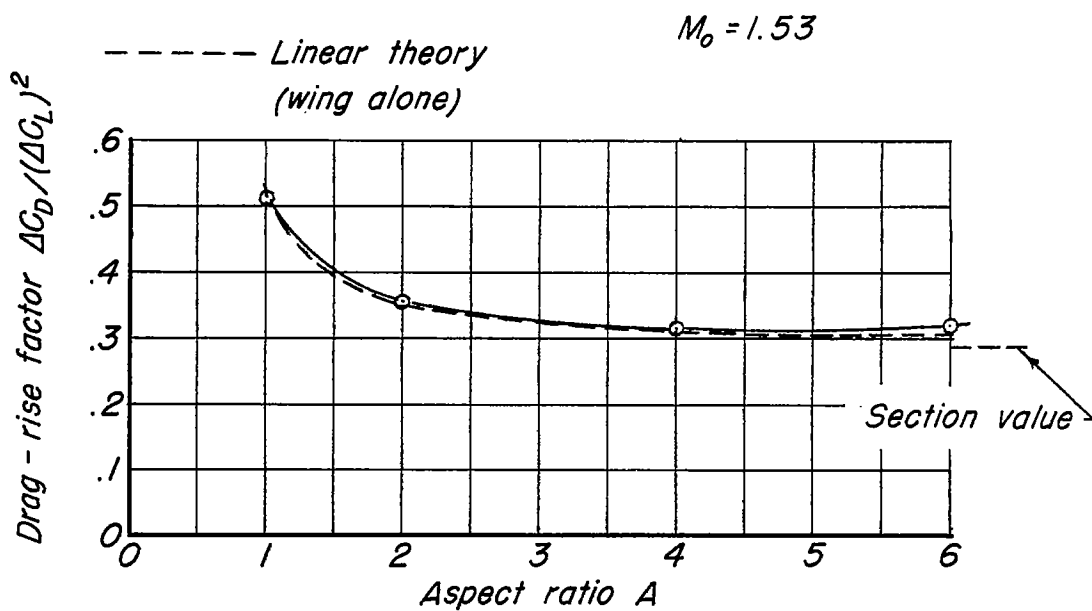


(b) Lift coefficient for minimum drag.

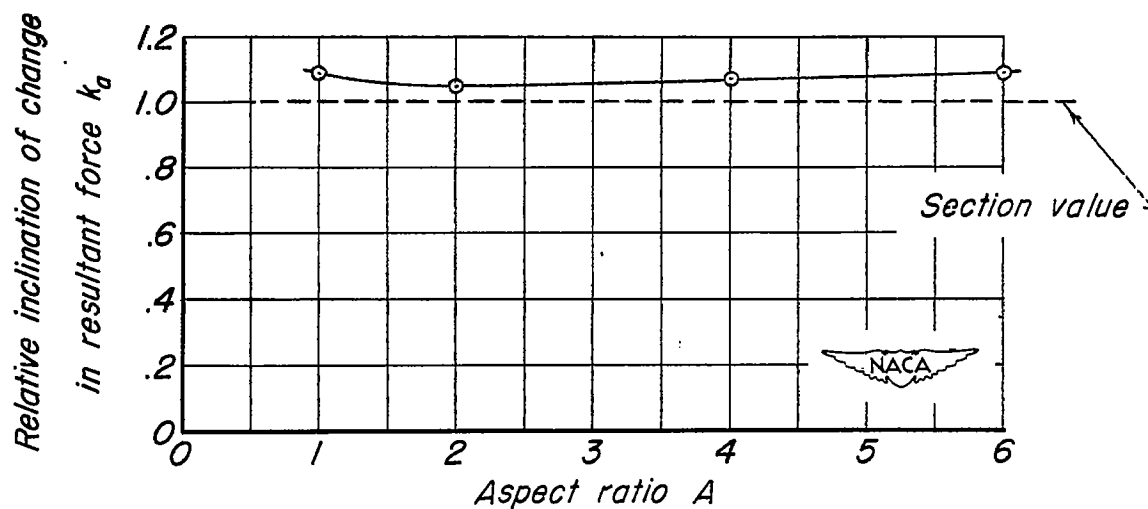
Figure 10.- Minimum-drag characteristics of taper-ratio series.

~~CONFIDENTIAL~~



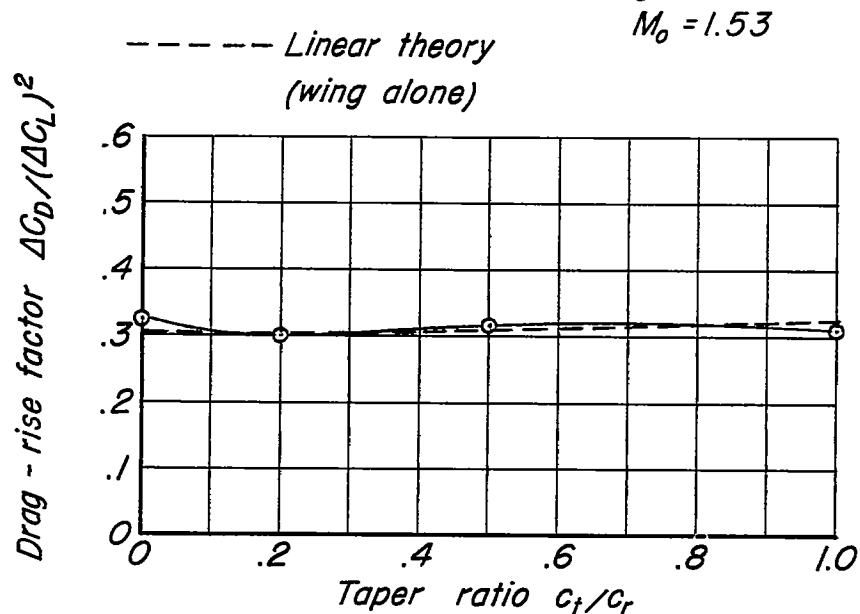


(a) Drag-rise factor.

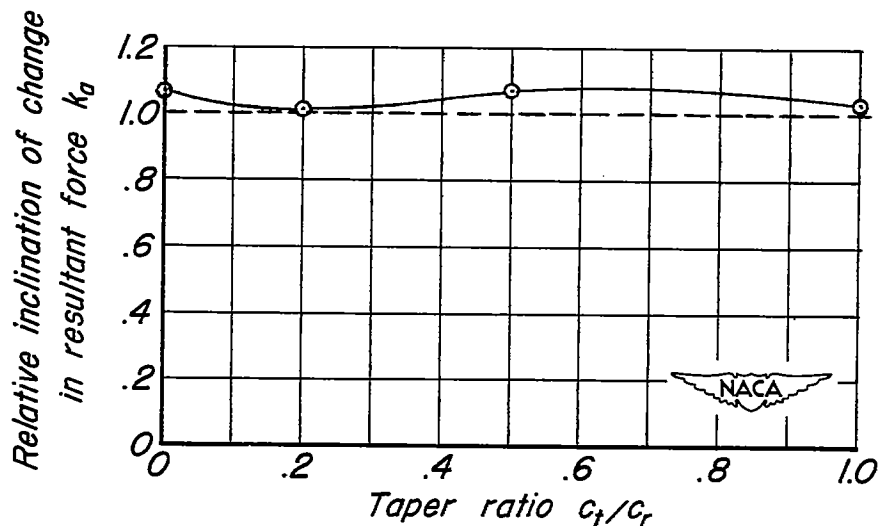


(b) Relative inclination of change in resultant force.

Figure 11.- Drag-rise characteristics of aspect-ratio series.



(a) Drag - rise factor.

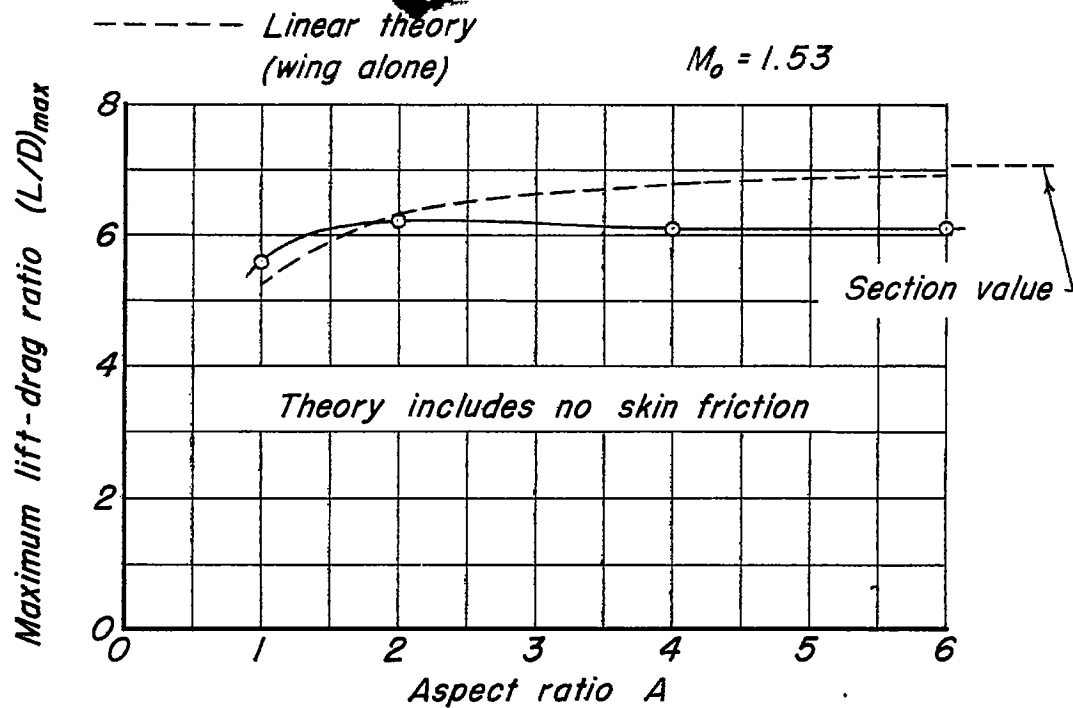


(b) Relative inclination of change in resultant force.

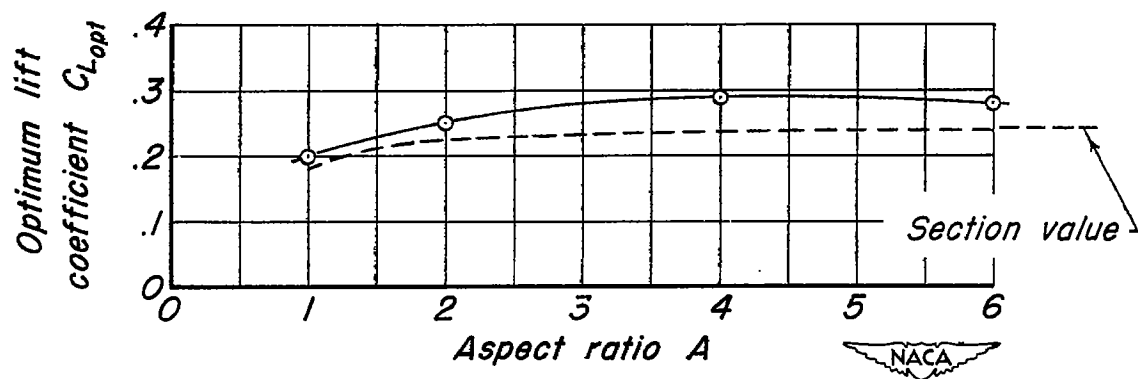
Figure 12.- Drag - rise characteristics of taper - ratio series.

CONFIDENTIAL

NACA RM No. A8E06



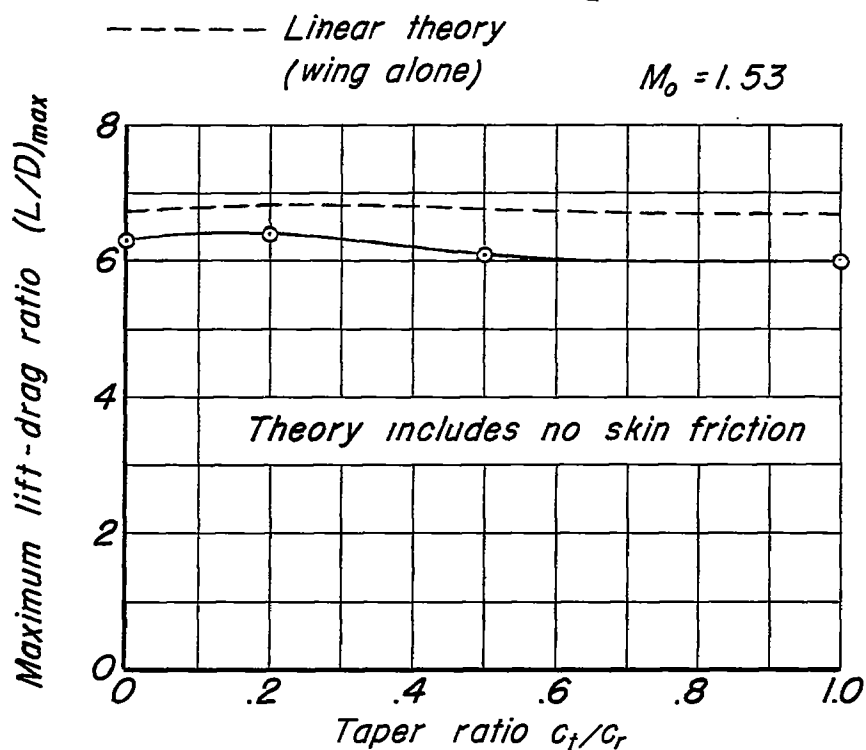
(a) Maximum lift-drag ratio.



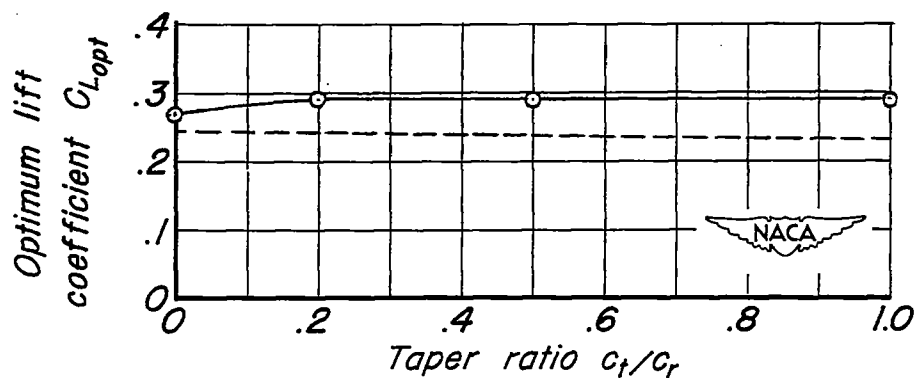
(b) Optimum lift coefficient.

Figure 13.- Maximum lift - drag characteristics of aspect - ratio series.

CONFIDENTIAL



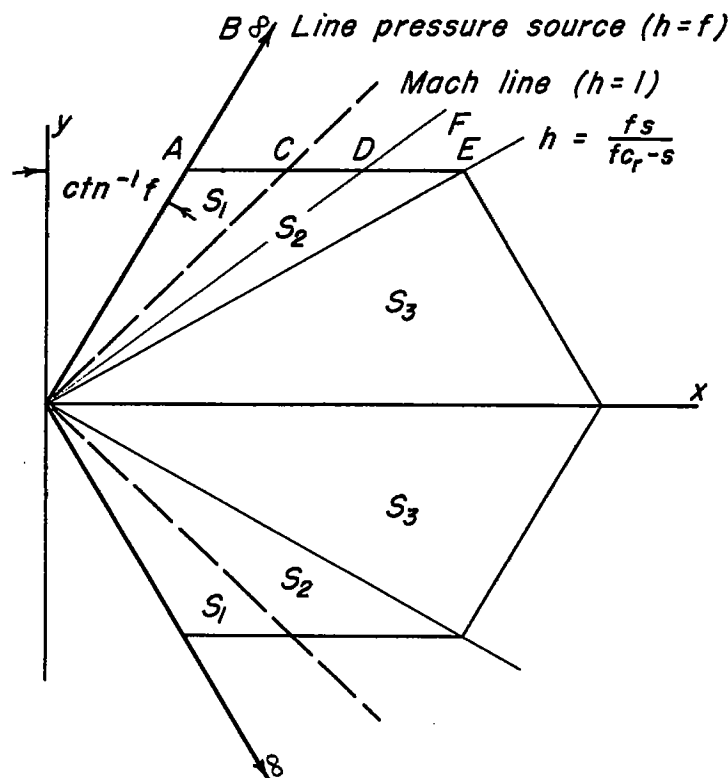
(a) Maximum lift-drag ratio.



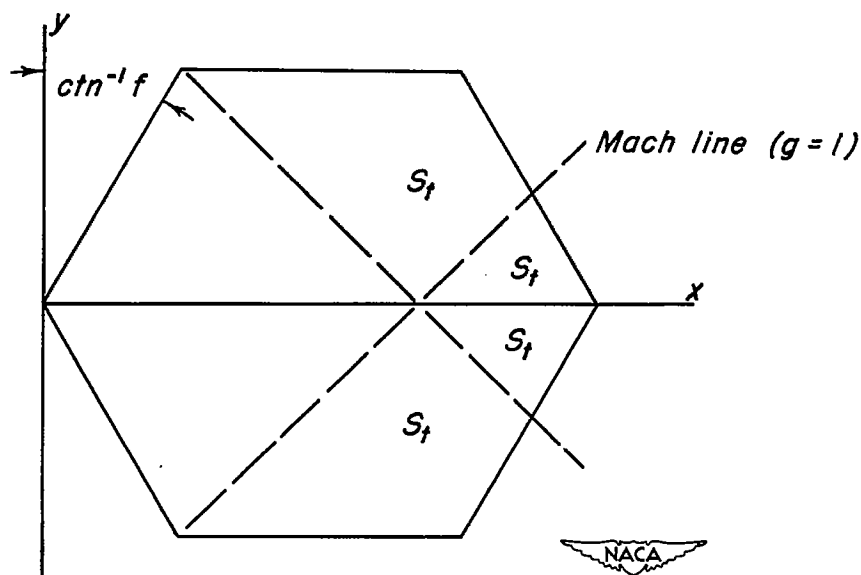
(b) Optimum lift coefficient.

Figure 14.- Maximum lift-drag characteristics of taper-ratio series.

CONFIDENTIAL



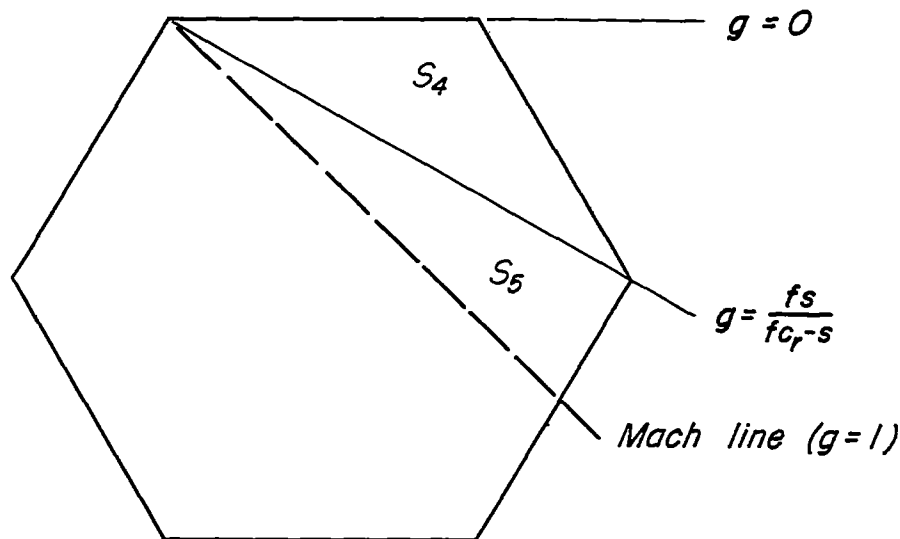
(a) Wing areas affected by primary loading



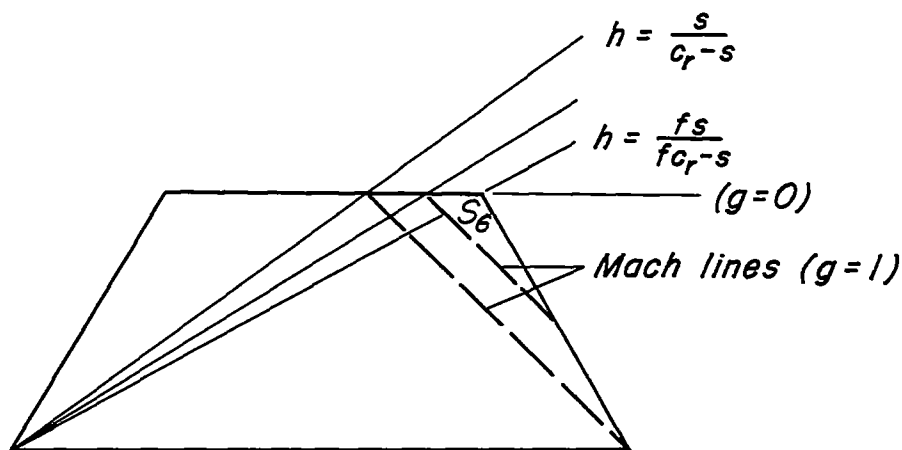
(b) Wing area affected by decremental loading

Figure 15.- Areas of wing U-4 affected by primary and decremental loadings.

~~CONFIDENTIAL~~



(a) Integration areas for first term of equation (A 16)

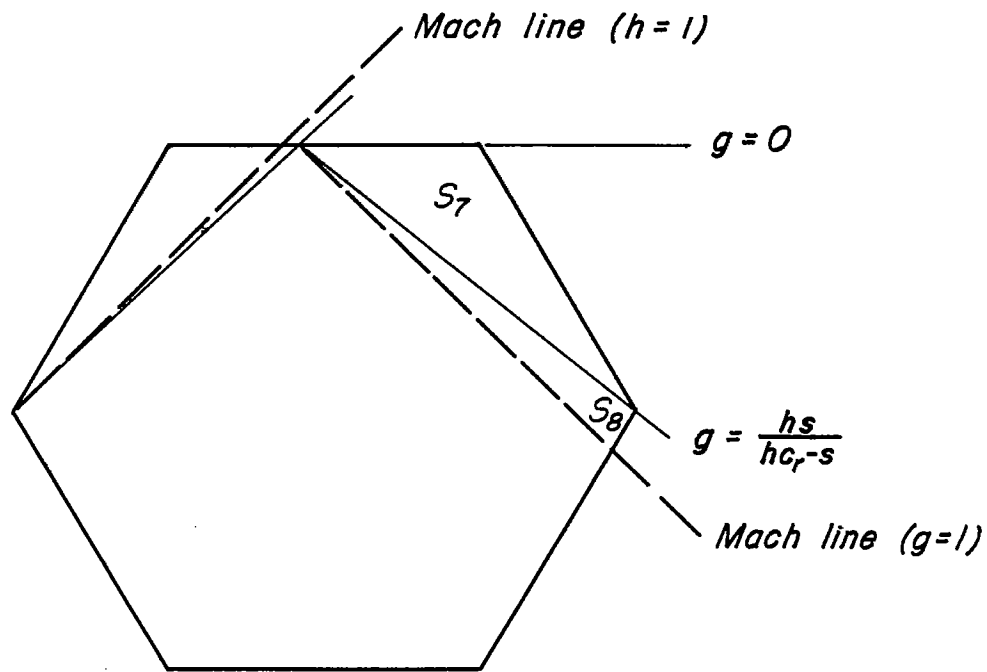


(b) Integration area for second term of equation (A 16)

$$\frac{s}{c_r - s} \geq h \geq \frac{fs}{fc_r - s}$$

Figure 16.- Integration areas and limits for equation (A 16).

~~CONFIDENTIAL~~



(c) Integration areas for second term of equation (A 16)

$$1 \geq h \geq \frac{s}{c_r - s}$$

Figure 16. - Concluded.